RESEARCH ARTICLE | JULY 07 2023

Theoretical investigation of the triggering of neoclassical tearing modes by transient resonant magnetic perturbations in NSTX FREE

R. Fitzpatrick ; Rajesh Maingi ; Jong-Kyu Park ; Steve Sabbagh

Physics of Plasmas 30, 072505 (2023)
https://doi.org/10.1063/5.0155038

Theoretical investigation of the triggering of neoclassical tearing modes by transient resonant magnetic perturbations in NSTX

Cite as: Phys. Plasmas **30**, 072505 (2023); doi: 10.1063/5.0155038
Submitted: 17 April 2023 · Accepted: 18 June 2023 ·
Published Online: 7 July 2023

R. Fitzpatrick,[1,a)] Rajesh Maingi,[2] Jong-Kyu Park,[2] and Steve Sabbagh[3]

AFFILIATIONS

[1]Institute for Fusion Studies, Department of Physics, University of Texas at Austin, Austin, Texas 78712, USA
[2]Princeton Plasma Physics Laboratory, Princeton University, Princeton, New Jersey 08544, USA
[3]Department of Applied Physics and Applied Mathematics, Columbia University, New York, New York 10027, USA

[a)]Author to whom correspondence should be addressed: rfitzp@utexas.edu

ABSTRACT

The extended perturbed equilibrium code asymptotic matching code is used to simulate the triggering of $n=1$ neoclassical tearing modes (NTMs) by a pulsed, rotating, $n=1$, resonant magnetic perturbation (RMP) in two example NSTX discharges. Although the two discharges are significantly different from one another, the results of the two sets of simulations are quite similar. The critical $n=1$ RMP pulse amplitude required to trigger an $n=1$ NTM is minimized when the RMP pulse rotation frequency matches the linear natural frequency of an $n=1$ tearing mode, resonant within the plasma, that is metastable to an NTM. However, if there is a frequency mismatch, then the seed magnetic island chain driven at the relevant resonant surface is forced to rotate with respect to the RMP, because the RMP pulse amplitude is nowhere near sufficient to lock the island chain to the RMP. This rotation causes the critical RMP pulse amplitude required to trigger an NTM to oscillate as the RMP pulse duration is varied. The critical amplitude is minimized when the RMP pulse duration is such that seed island chain executes a half-integer number of rotations with respect to the pulse. All of the minima have the same value.

I. INTRODUCTION

Neoclassical tearing modes (NTMs) are the main obstacle to obtaining normalized plasma pressure (β) levels in tokamak[1] plasmas that are adequate for the achievement of thermonuclear fusion.[2,3] NTMs were originally identified experimentally on the TFTR tokamak.[4] NTMs lead to the development of low poloidal and toroidal mode number (m and n) magnetic island chains on toroidal magnetic flux-surfaces within the plasma that are characterized by rational (i.e., m/n) values of the safety-factor (q). An NTM is driven by a helical reduction in the bootstrap current[5] profile that arises as a consequence of the flattening of the plasma pressure across the associated island chain region.[6] However, a magnetic island chain can only locally flatten the plasma pressure when its radial width exceeds a certain threshold value that depends on the local ratio of the parallel and perpendicular energy diffusivities.[7] This observation leads to the conclusion that NTMs are actually metastable. In other words, some sort of seed perturbation must be applied to the relevant rational magnetic flux-surface in order to trigger an NTM. In practice, the seed perturbation usually takes the form of a transient magnetic perturbation that is resonant at the rational surface.[8,9] Such perturbations are generated in tokamak plasmas primarily by sawtooth crashes, edge localized modes (ELMs), and fishbones.[2,3]

The aim of this paper is to investigate how the properties (i.e., amplitude, duration, and rotation frequency) of a transient resonant magnetic perturbation (RMP) applied to a toroidal tokamak plasma affect its ability to trigger NTMs within the plasma. In this study, we shall use the extended perturbed equilibrium code (EPEC) (see Sec. II) to simulate what happens when a transient $n=1$ magnetic perturbation is applied to a typical NSTX plasma.

II. BRIEF DESCRIPTION OF THE EPEC CODE

The EPEC code[10–13] employs an asymptotic matching[14–24] approach to determine the resistive response of a toroidal tokamak equilibrium to an applied RMP. The main advantage of the asymptotic matching approach is that it largely removes the very short Alfvén time from the problem. In fact, the EPEC code is capable of accurately simulating the resistive response of a toroidal tokamak plasma to an RMP while taking time steps that extend over many Alfvén times.

In this manner, the code is able to simulate the full duration of a plasma discharge in a matter of minutes of real time.

The version of the EPEC model used in this paper is described in detail in the Appendix. The EPEC model is fully toroidal and makes use of experimental magnetic equilibrium data and plasma profile data. The homogenous component of the toroidal tearing stability matrix is calculated approximately by the EPEC code. The inhomogeneous component of the matrix, which specifies the ideal response of the plasma to the applied RMP, is calculated exactly by the GPEC code. (see subsection 2 d of the Appendix). The model incorporates an accurate neoclassical model[25] that takes impurities and neutral particles into account and allows the calculation of the neoclassical poloidal flow-damping timescale, the charge-exchange damping timescale, the neoclassical ion rotation profile, and the bootstrap current profile (see subsection 3 of the Appendix). The responses of the various resonant layers in the plasma are calculated by interpolating between the linear and nonlinear response regimes. The linear response model includes diamagnetic flows, the ion sound radius, and anomalous perpendicular momentum and energy transport. The nonlinear response model includes perturbed bootstrap current, magnetic field-line curvature, ion polarization current, and island saturation terms in the generalized Rutherford equation (see subsection 4 of the Appendix). The EPEC model accurately calculates the (theoretical) critical island widths needed to locally flatten the plasma pressure profile (see subsection 4 c of the Appendix). The switch-over between the linear and the nonlinear response models occurs when the island width exceeds the critical island width.

The *natural frequency* of a tearing mode, resonant within the plasma, is a concept that plays a central role in the EPEC model, and is, therefore, worth discussing. The natural frequency of a stable, or metastable (prior to triggering), tearing mode is defined as the angular frequency at which the mode would rotate if it had a finite amplitude (in the absence of the RMP).[19] The natural frequency is determined by a combination of $\mathbf{E}\times\mathbf{B}$ and diamagnetic plasma flows at the rational surface. The natural frequency of a tearing mode can be calculated exactly in two regimes; first, the *linear* regime, in which the island width is much smaller than the linear layer width; second, the *nonlinear* regime, in which the island width is much greater than the linear layer width (and the critical island width above which the plasma pressure is locally flattened). According to the linear tearing mode theory, the natural frequency is such that the tearing mode is essentially convected by the *electron* fluid at the rational surface.[17,26,27] On the other hand, according to the nonlinear tearing mode theory, the tearing mode is essentially convected by the *ion* fluid at the rational surface.[28] To be more exact, under the influence of neoclassical poloidal flow damping, a nonlinear tearing mode is forced to rotate in the ion diamagnetic direction with respect to the local $\mathbf{E}\times\mathbf{B}$ frame, but in the electron diamagnetic direction with respect to the local ion fluid frame, the exact rotation frequency is being influenced by plasma impurities.[29–31] The EPEC model interpolates between these two possibilities, with the switchover from the linear to the nonlinear natural frequency being triggered by the flattening of the local temperature and density profiles at the rational surface (see subsection 5 b of the Appendix). As will become apparent, it is the linear natural frequency that controls the triggering of NTMs by rotating RMPs.

III. FIRST EXAMPLE NSTX DISCHARGE

A. Introduction

The two example NSTX discharges studied in this paper were chosen because they were both fairly generic and had precomputed kinetic-EFITs.

The first example discharge is 127317, which was a discharge used in an investigation of the interaction between edge localized modes (ELMs) and RMPs in NSTX.[32] Discharge 127317 is an H-mode plasma, characterized by a (almost) double magnetic null boundary shape, 6 MW of neutral beam heating power, and no fresh deposition of the lithium coating on the plasma-facing wall-tiles.

B. Magnetic equilibrium

Figure 1 shows the experimental magnetic equilibrium of NSTX discharge 127317 at $t = 400$ ms. This equilibrium is characterized by a scale major radius $R_0 = 0.85$ m (see subsection 2 a of the Appendix), a scale toroidal magnetic field-strength $B_0 = 0.44$ T (see subsection 2 b of the Appendix), a net toroidal plasma current $I_\phi = 753$ kA, a safety-factor at the 95% flux-surface $q_{95} = 11.0$, and a poloidal beta $\beta_p = 0.61$.

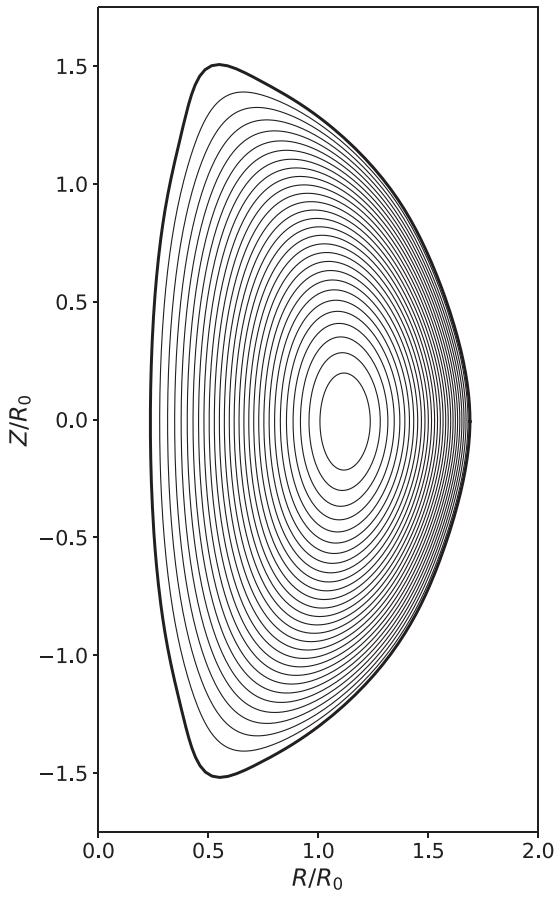

FIG. 1. Equilibrium magnetic flux-surfaces in NSTX discharge 127317 at $t = 400$ ms. Here, $R_0 = 0.85$ m.

C. Plasma profiles

Figure 2 shows the experimental safety-factor, electron number density, electron temperature, ion temperature, impurity ion number density, and impurity ion toroidal angular velocity profiles in NSTX discharge 127317 at $t = 400$ ms. The majority ions are deuterium, and the impurities are assumed to be fully-stripped carbon ions (with the same temperature as the majority ions), which permits the $Z_{\rm eff}$ profile to be determined from the profile data (see subsection 3 a of the Appendix). Note that the discharge is subject to rotation braking due to an applied $n = 3$ RMP,[33] which accounts for its slightly lower than usual toroidal rotation (compare the rotation in Fig. 12). Because there is no poloidal impurity ion rotation data for this discharge, the $\mathbf{E} \times \mathbf{B}$ rotation profile is deduced from the toroidal impurity ion rotation data using neoclassical theory (see subsection 3 g of the Appendix).

The perpendicular electron energy diffusivity (χ_e), perpendicular ion energy diffusivity (χ_i), perpendicular toroidal momentum diffusivity (χ_ϕ), and perpendicular particle diffusivity ($D_\perp$) are given the plausible values 1.0, 1.0, 1.0, and 0.2 $\rm m^2/s$, respectively, throughout the plasma. It turns out that the simulations presented in this paper are not particularly sensitive to these values.

Note that neutrals do not really play a role in the physics of NTMs, which are resonant in the plasma core, and are only included in the calculation because they need to be specified in the EPEC model. The flux-surface averaged neutral deuterium atom number density takes the form $\langle n_n \rangle(r) = \langle n_n \rangle(r_{100})/[1 + (r - r_{100})^2/l_n^2]$, where $\langle n_n \rangle(r_{100}) = 1.0 \times 10^{16}\,\rm m^{-3}$, and $l_n = 1.3 \times 10^{-2}\,\rm m$. The flux-surface neutral poloidal asymmetry parameter is given the value $y_n = 1.5$ (see subsection 3 e of the Appendix). The flux-surface averaged deuterium-atom/deuterium-ion charge-exchange rate constant is $\langle \sigma\, v \rangle_i^{\rm cx} = 4 \times 10^{-14}\,\rm m^3\,s^{-1}$.[34] The neutrals are assumed to be hot (i.e., $E_n/T_i = 1.$).

D. $n = 1$ natural frequencies

Figure 3 shows the linear natural frequencies [i.e., the ϖ_{ek} defined in Eq. (A142)] of all of the $n = 1$ tearing modes resonant within discharge 127317. There are 18 such modes, with poloidal mode numbers lying in the range $m = 2$ to $m = 19$. As is usual in a tokamak discharge with co-injected neutral beam heating, the tearing modes resonant in the edge pressure gradient region (the pedestal) have large positive natural frequencies (which implies that they would rotate in the electron diamagnetic direction were they naturally unstable) as a consequence of relatively strong edge electron diamagnetic rotation (in this case, mostly due to the comparatively large electron density gradient in the pedestal) and relatively weak edge toroidal plasma rotation. On

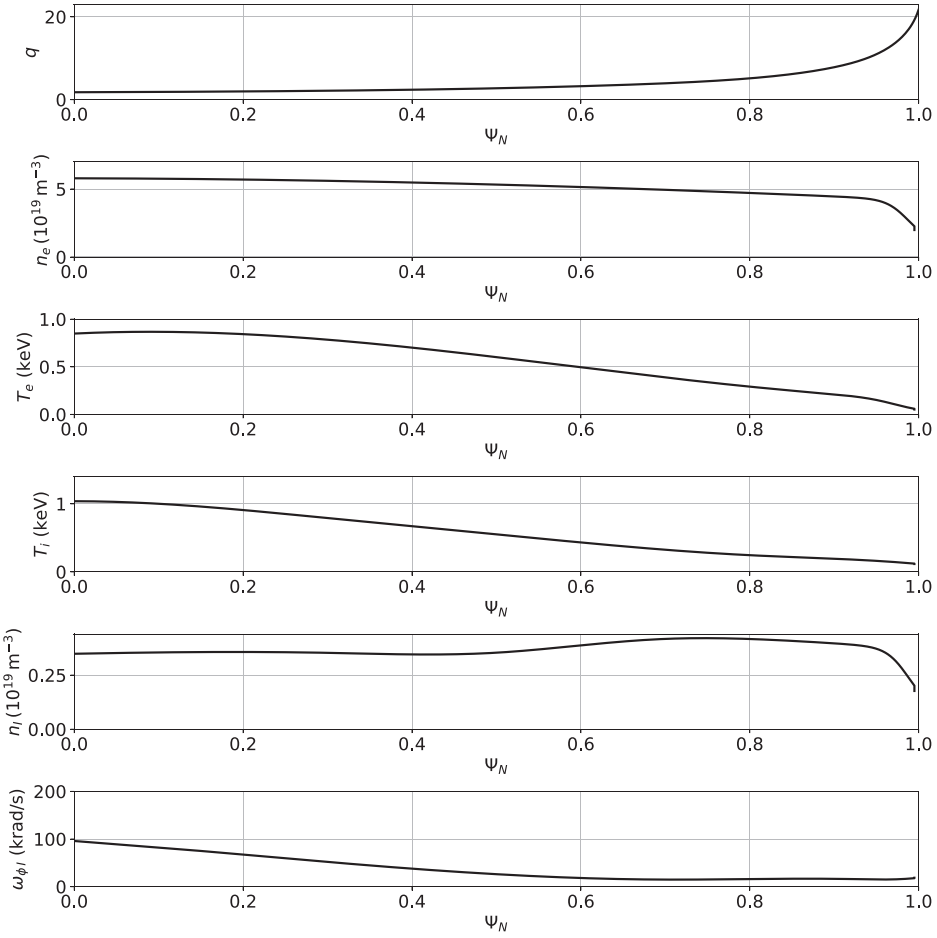

FIG. 2. Safety-factor, electron number density, electron temperature, ion temperature, impurity ion number density, and impurity ion toroidal rotation profiles in NSTX discharge 127317 at $t = 400$ ms.

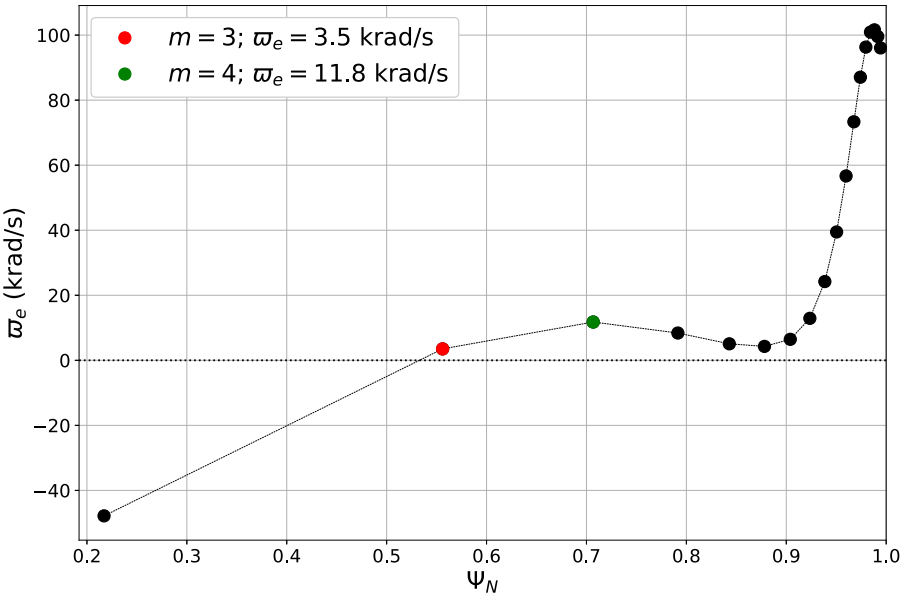

FIG. 3. Linear $n=1$ natural frequencies in NSTX discharge 127317. There are 18 $n=1$ resonant surfaces in the plasma corresponding to $m=2$ through $m=19$. Only the $m=3$ and $m=4$ surfaces are potentially unstable to NTMs.

the other hand, the tearing modes resonant in the core have large negative natural frequencies (which implies that they would rotate in the ion diamagnetic direction were they naturally unstable) as a consequence of relatively strong core toroidal plasma rotation (in the same direction as the toroidal plasma current) and comparatively weak core electron diamagnetic rotation.[13] Possibly because of the rotation braking, there is a wide region lying between the pedestal and the core where the natural frequencies hover close to zero. Moreover, the natural frequency curve (i.e., the curve that interpolates between the natural frequencies) crosses zero (i.e., switches direction), about halfway between the magnetic axis and the last closed magnetic flux-surface (LCFS). [At the zero-crossing, the tendency of electron diamagnetic rotation to make the natural frequency positive is exactly balanced by the tendency of toroidal plasma rotation (in the same direction as the toroidal plasma current) to make the natural frequency negative.] In a conventional aspect-ratio tokamak plasma, the zero-crossing is invariably at the top of the pedestal.[10] The observation that the zero-crossing of the $n=1$ natural frequency curve in NSTX does not take place at the top of the pedestal (see also Fig. 13) may help to explain why RMPs were unable to suppress ELMs in this device.[32] (Admittedly, the ELM suppression experiments were performed with an $n=3$ RMP, but the location of the zero-crossing for the $n=3$ curve is identical to that for the $n=1$ curve.) It should be noted that the fact that the natural frequency curve of tearing modes, resonant within H-mode plasmas in conventional aspect-ratio tokamaks heated by co-injected neutral beams, invariably passing through zero close to the top of the pedestal is an important ingredient in recent theories of how RMP-induced ELM suppression works.[10–13,35]

E. $n=1$ NTM stability

Only two of the $n=1$ tearing modes resonant in discharge 127317 are metastable to NTMs. These modes are resonant in the middle of the plasma, close to the zero-crossing of the natural frequency curve. The unstable modes are the $m=3$, with a natural frequency of 3.5 krad/s, and the $m=4$, with a natural frequency of 11.8 krad/s. Figure 4 shows the right-hand sides (RHSs) of the modified Rutherford island width evolution equations for the $m=3$ and $m=4$ modes as functions of island width. [In fact, what is plotted is $E_{kk}+f_k$. See Eqs. (A3) and (A107). E_{kk} is the (negative) classical tearing stability index, which is only calculated approximately for low-m modes by EPEC. f_k specifies the destabilizing effect of the perturbed bootstrap current, the stabilizing effect of magnetic field-line curvature, the stabilizing effect of the ion polarization current, and the stabilizing effect of island saturation. All of these effects are calculated accurately by EPEC.] As expected for a metastable NTM, both RHS curves shown in Fig. 4 are negative for small and large island widths and positive for intermediate island widths. The smaller zero-crossing of the RHS curve indicates the width of the seed island chain that must be induced at the resonant (i.e., rational) surface in order to trigger the NTM. The larger zero-crossing indicates the saturated width of the NTM. It should be noted that the RHS curves for all the other $m=1$ modes resonant in discharge 127317 are negative for all island widths (which indicates NTM stability).

F. $n=1$ RMP

For the sake of definiteness and convenience, the $n=1$ transient rotating RMP that is used to (theoretically) trigger $n=1$ NTMs in discharge 127317 is generated by pulsing a rotating $n=1$ current in the RMP coils installed on NSTX. (To be more exact, the ideal response of the plasma to the currents flowing in the RMP coils is calculated by the GPEC code,[36] and this information is used as the basis for the EPEC calculation. See subsection 2 d of the Appendix.) An RMP produced in this manner is supposed to represent the type of rotating, multi-harmonic RMP that would be generated by a sawtooth crash or an ELM. For this reason, we do not take into account the shielding effect of eddy currents induced in the vacuum vessel (because the real RMPs that trigger NTMs are generated inside the plasma, and are,

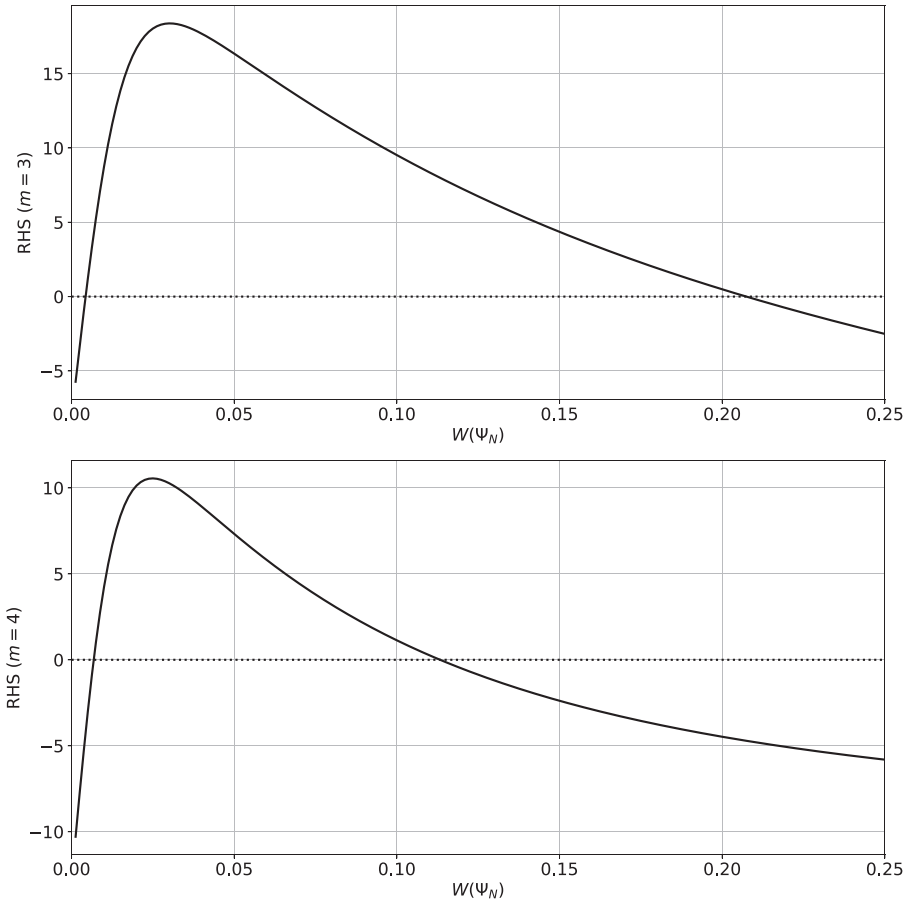

FIG. 4. Right-hand sides of the modified Rutherford equations for the $m = 3/n = 1$ and $m = 4/n = 1$ tearing modes in NSTX discharge 127317 at $t = 400$ ms.

therefore, not strongly shielded from the remainder of the plasma by vacuum vessel eddy currents).

G. Triggering of $n = 1$ NTMs

Figure 5 shows the $n = 1$ island widths vs time driven in discharge 127317, as calculated by the EPEC code, in response to an $n = 1$ current pulse of amplitude 0.089 kA, duration 5 ms, and frequency 0 krad/s applied to the RMP coils. It can be seen that an NTM is not triggered (because all of the island widths eventually decay to zero after the pulse is applied).

Figure 6 shows the $n = 1$ island widths vs time driven in discharge 127317 in response to an $n = 1$ current pulse of slightly larger amplitude 0.090 kA, duration 5 ms, and frequency 0 krad/s applied to the RMP coils. It can be seen that the $m = 3$ NTM is triggered. In other words, the $m = 3$ island width grows and eventually saturates at a large value. Note that most of the growth occurs long after the application of the RMP, indicating that something other than the RMP (i.e., the perturbed bootstrap current) is responsible for driving the growth. To be more exact, it is inferred that the RMP pushes the $m = 3$ island above the seed value shown in Fig. 4 (i.e., the smaller zero-crossing of the RHS curve in the top panel), allowing the perturbed bootstrap current to drive the further growth in the island width by itself. Because all of the $n = 1$ tearing modes resonant in the plasma are coupled together, the growth of the $m = 3$ NTM drives narrow island chains at the $m = 4$, $m = 5$, and $m = 6$ resonant surfaces. However, these are not NTMs.

Figure 7 shows the natural frequency and phase velocity of the $m = 3$ NTM triggered in the previous figure vs time. Note that the plasma is subject to a small-amplitude, static, background RMP in order to ensure that the various modes in the calculation have reproducible initial phases. Prior to the application of the transient RMP, there is a very small stationary magnetic island chain driven at the $m = 3$ resonant surface. The fact that the phase velocity and natural frequency of the mode do not match indicates that the plasma at the resonant surface is capable of freely flowing through the locked island chain (because of its very small width). As soon as the transient RMP is applied to the plasma, a seed island chain is driven at the resonant surface. This island chain is sufficiently wide that it is dragged by the plasma at the resonant surface, causing it to rotate in the direction of its natural frequency. The rotation is braked by the RMP, which means that the phase velocity of the seed island chain does not match its natural frequency. The fact that the natural frequency barely changes during the application of the transient RMP indicates that the amplitude of the RMP is nowhere near large enough to halt the plasma rotation at the resonant surface. As soon as the transient RMP disappears, the seed island chain is no longer braked by the RMP, and consequently accelerates until it is rotating at its natural frequency. As the seed island chain grows and becomes a fully fledged NTM, its natural frequency

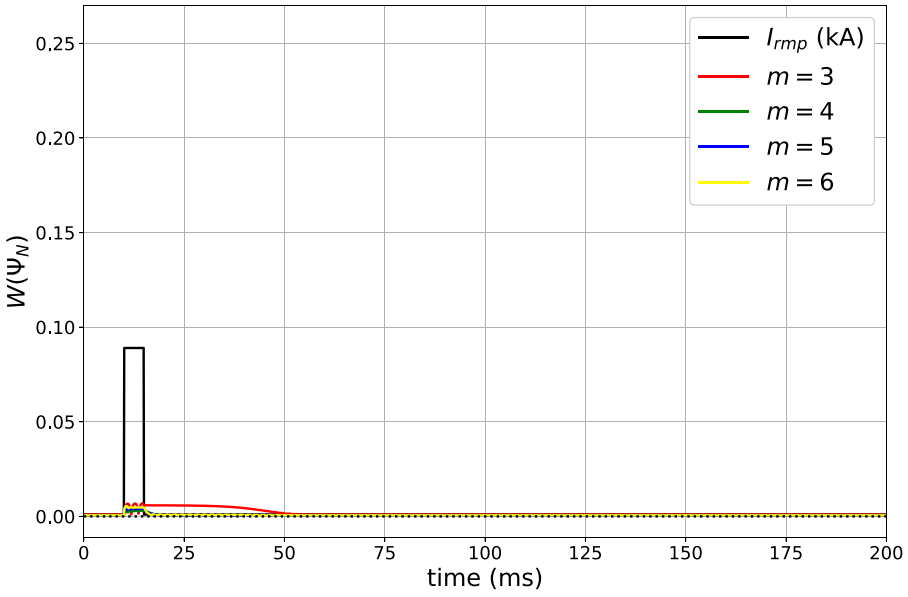

FIG. 5. Calculated $n = 1$ island widths vs time in NSTX discharge 127317 in response to an $n = 1$ current pulse of amplitude 0.089 kA, duration 5 ms, and frequency 0 krad/s applied to the RMP coils.

changes because it switches from that characteristic of a linear layer (in this case, small and positive) to that characteristic of a nonlinear magnetic island chain (in this case, large and negative) (see subsection 5 b of the Appendix). However, this switch takes place long after the triggering of the NTM, which suggests that it is the linear, rather than the nonlinear, natural frequency that plays a role in NTM triggering.

H. Pulse duration scan

Figure 8 shows the critical $n = 1$ RMP current pulse amplitude required to trigger an $m = 3$ NTM in discharge 127317 as a function of the pulse duration for various different pulse frequencies.

The figure was generated as follows: For a given pulse duration and frequency, an RMP pulse of a certain amplitude was applied to the plasma, and the plasma response was simulated for 200 ms using the EPEC code, after which a determination was made as to whether or not an NTM had been triggered. A bisection search was made in the pulse amplitude in order to determine the critical amplitude needed to trigger the NTM. In general, it required about ten EPEC simulations to determine the critical amplitude. Because there are about 800 points in each curve plotted in the figure, and there are five curves, it follows that the production of the figure required about 40 000 EPEC simulations (which means that a total of about 8000 s of plasma dynamics was simulated). Obviously, this would be impossible

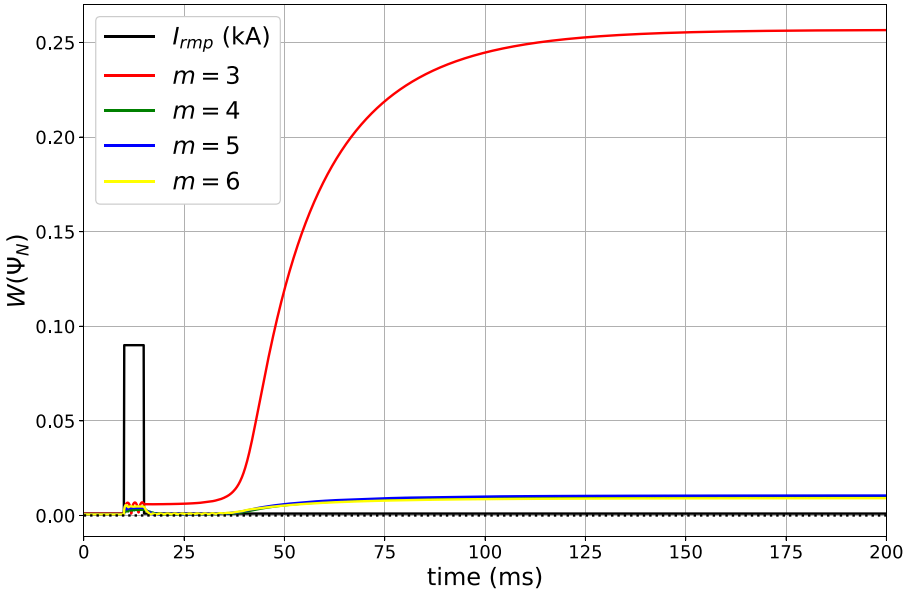

FIG. 6. Calculated $n = 1$ island widths vs time in NSTX discharge 127317 in response to an $n = 1$ current pulse of amplitude 0.090 kA, duration 5 ms, and frequency 0 krad/s applied to the RMP coils.

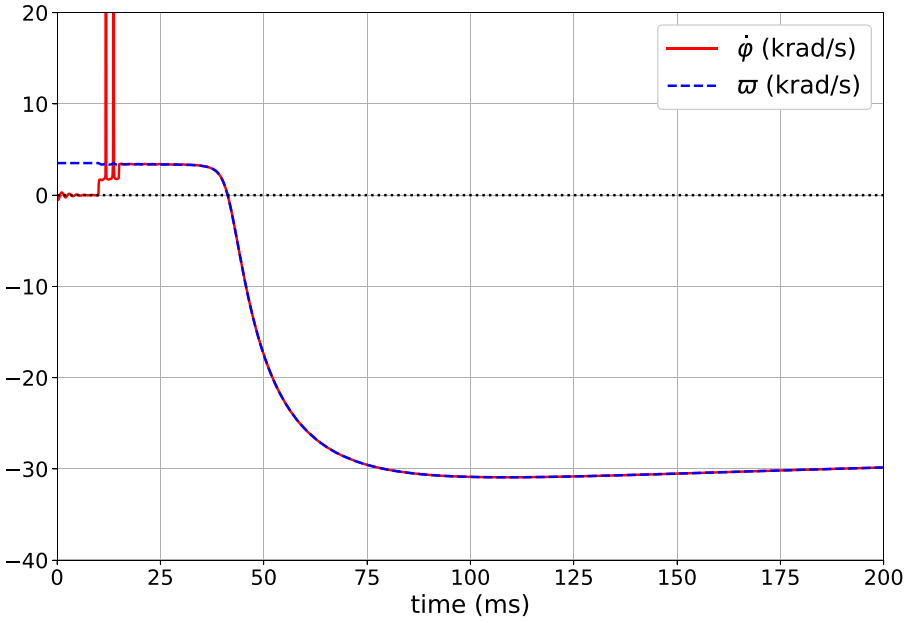

FIG. 7. Calculated phase velocity ($\dot{\varphi}$) and natural frequency (ϖ) of the $m = 3/n = 1$ tearing mode vs time in NSTX discharge 127317 in response to an $n = 1$ current pulse of amplitude 0.090 kA, duration 5 ms, and frequency 0 krad/s applied to the RMP coils.

using a conventional MHD code. However, it is perfectly feasible using an asymptotic matching code.

Let us concentrate, first, on the green curve, which corresponds to zero-frequency current pulses. One might expect that the critical pulse amplitude required to trigger an NTM would decrease monotonically with pulse duration, because a longer pulse would generate a wider seed island chain. In fact, this is not the case, and the pulse amplitude curve exhibits oscillations. The key to understanding this unexpected behavior is the fact that the seed island chain is not locked to the RMP pulse, but is instead forced to rotate with respect to the pulse by the plasma rotation at the resonant surface (see Fig. 7). This means that after a time sufficient for the seed island chain to perform half a rotation with respect to the pulse, the seed island width attains a maximum value (because, assuming that it was initially in phase with the pulse, it is now in phase quadrature). Hence, the critical pulse amplitude attains a minimum value. A longer pulse can make the seed island width smaller, but not larger. Thus, the minimum pulse amplitudes (which are all the same) correspond to pulse durations that allow the seed island chain to execute 1/2, 3/2, 5/2, and many other rotations with respect to the pulse. The time needed for the seed island chain to execute a full rotation with respect to the pulse is inversely proportional to the difference between the pulse frequency and the linear

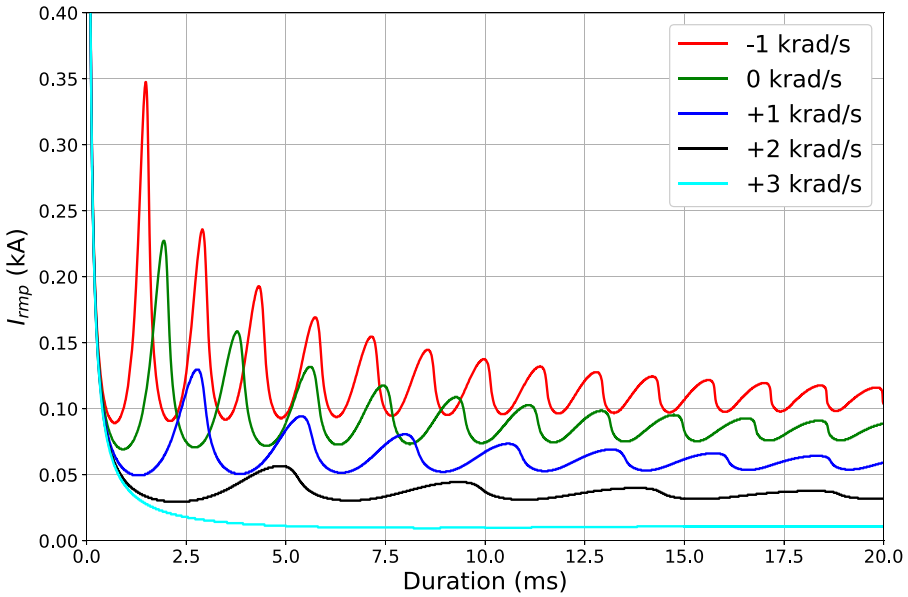

FIG. 8. Critical $n = 1$ RMP coil current pulse amplitude required to trigger an NTM in NSTX discharge 127317 as a function of the pulse duration for various different pulse frequencies.

natural frequency at the resonant surface. Thus, when the pulse frequency (almost) matches the linear natural frequency (light-blue curve—in this case, the frequency mismatch is only 0.5 krad/s) the rotation time is (almost) infinite, and the critical pulse amplitude exhibits the expected monotonic decrease with pulse duration. On the other hand, as the frequency mismatch increases (see the sequence from the black to the dark-blue, to the green, to the red, curve) the oscillations in the critical pulse amplitude become shorter and more violent.

Note that at very short pulse durations, the critical pulse amplitude needed to trigger an NTM becomes independent of the pulse frequency. However, it is clear from the figure that very short duration pulses are relatively inefficient at triggering NTMs. (In fact, in the short pulse duration limit, the critical pulse amplitude scales as the inverse of the pulse duration.)

I. Pulse frequency scan

Figure 9 shows the critical $n=1$ RMP current pulse amplitude required to trigger an NTM in discharge 127317 as a function of the pulse frequency for a pulse duration of 20 ms. The generation of this figure required about 20 000 EPEC simulations. As might be expected, the critical pulse amplitude exhibits a minimum value (which is not quite zero) when the pulse frequency matches the linear natural frequency of the $m=3$ tearing mode. The critical pulse amplitude increases in a roughly linear fashion, with superimposed oscillations of increasing amplitude, as the size of the frequency mismatch increases. The critical pulse amplitude exhibits a secondary minimum when the pulse frequency matches the linear natural frequency of the $m=4$ tearing mode. This is a synergistic effect by which the pulse simultaneously triggers both an $m=3$ and an $m=4$ NTM. This process is illustrated in Fig. 10, which shows what happens when a pulse whose frequency closely matches the linear natural frequency of the $m=4$ tearing mode is applied to the plasma. It can be seen that an $m=4$ NTM is almost immediately triggered, closely followed by an $m=3$ NTM. Both NTMs grow to large amplitudes and clearly drive smaller island chains at other resonant surfaces in the plasma. It should be noted that the pulse amplitudes in Figs. 5 and 10 are the same; it is only the pulse frequencies that are different. Thus, a comparison of the two figures reveals that merely changing the pulse frequency can cause the completely benign plasma response shown in Fig. 5 to convert into the catastrophic response shown in Fig. 10.

IV. SECOND EXAMPLE NSTX DISCHARGE

A. Introduction

The second example NSTX discharge studied in this paper is 139057, which was a discharge used in an investigation of blob dynamics in NSTX.[37] Discharge 139057 is an H-mode plasma, characterized by a single magnetic null boundary shape, 6 MW of neutral beam heating power, and fresh lithium coating of the wall-tiles.

B. Magnetic equilibrium

Figure 11 shows the experimental magnetic equilibrium of NSTX discharge 139057 at $t=557$ ms. This equilibrium is characterized by a scale major radius $R_0=0.85$ m, a scale toroidal magnetic field-strength $B_0=0.54$ T, a net toroidal plasma current $I_\phi=907$ kA, a safety-factor at the 95% flux-surface $q_{95}=9.5$, and a poloidal beta $\beta_p=0.57$.

C. Plasma profiles

Figure 12 shows the experimental safety-factor, electron number density, electron temperature, ion temperature, impurity ion number density, and impurity ion toroidal angular velocity profiles in NSTX discharge 139057 at $t=557$ ms. As before, the majority ions are deuterium, and the impurities are assumed to be fully stripped carbon ions. Note that the discharge is not subject to rotation braking due to an applied $n=3$ RMP, which accounts for the slightly higher toroidal rotation than that present in discharge 127317 (see Fig. 2). As before,

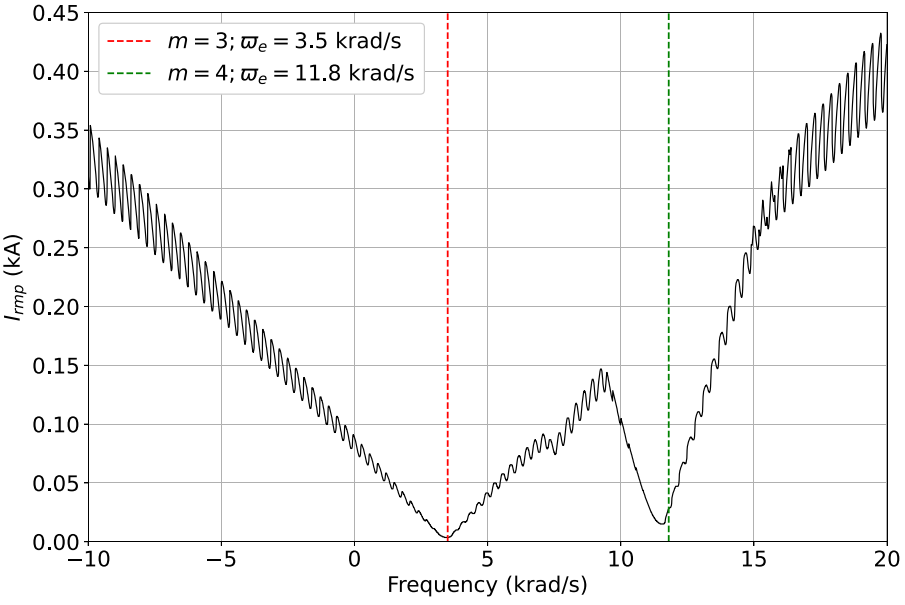

FIG. 9. Critical $n=1$ RMP coil current pulse amplitude required to trigger a NTM in NSTX discharge 127317 as a function of the pulse frequency for a pulse duration of 20 ms.

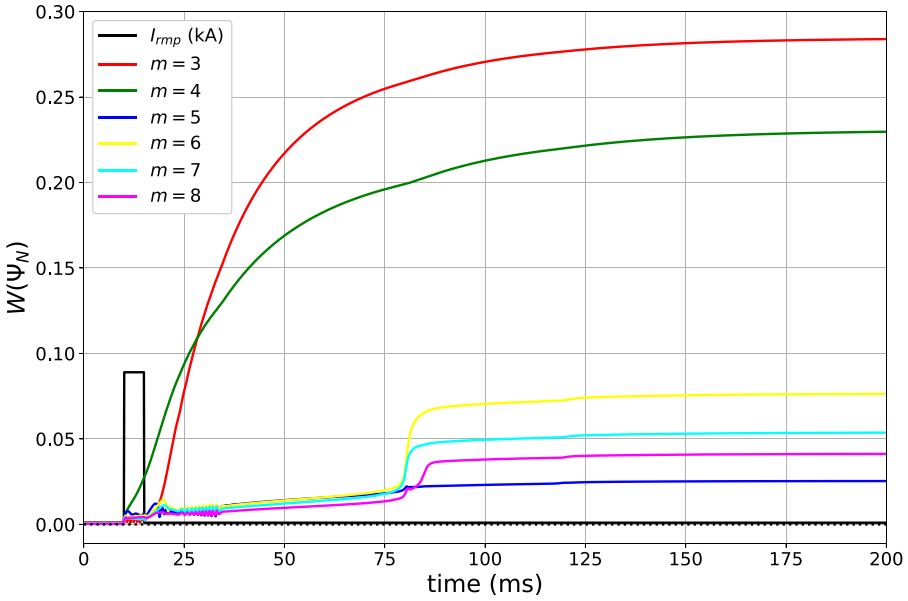

FIG. 10. Calculated $n = 1$ island widths vs time in NSTX discharge 127317 in response to an $n = 1$ current pulse of amplitude 0.089 kA, duration 5 ms, and frequency 11 krad/s applied to the RMP coils.

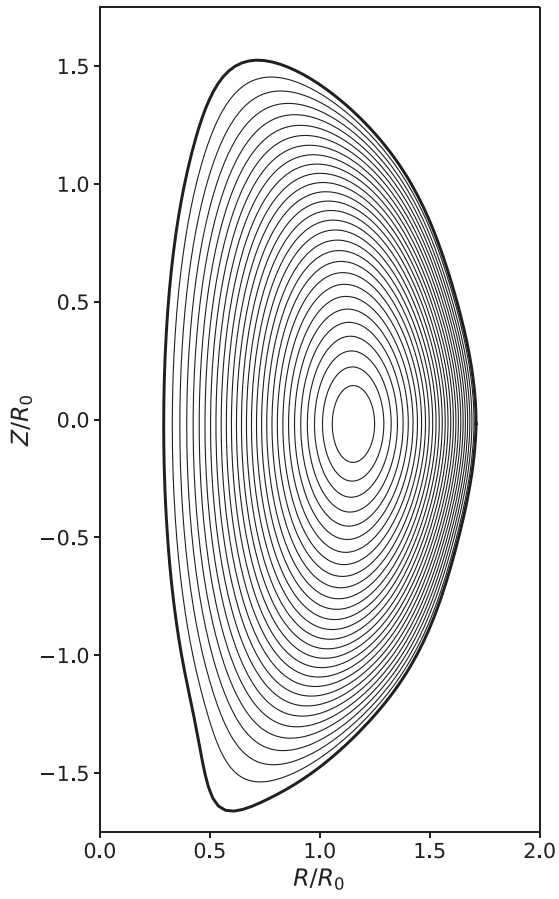

FIG. 11. Equilibrium magnetic flux-surfaces in NSTX discharge 139057 at $t = 557$ ms. Here, $R_0 = 0.85$ m.

the $\mathbf{E} \times \mathbf{B}$ rotation profile is deduced from the toroidal impurity ion rotation data using neoclassical theory.

The diffusivity and neutral profiles in discharge 139057 are assumed to be the same as those adopted in the study of discharge 127317.

D. $n = 1$ natural frequencies

Figure 13 shows the linear natural frequencies of all of the $n = 1$ tearing modes resonant within discharge 139057. There are 13 such modes, with poloidal mode numbers lying in the range $m = 2$ to $m = 14$. As is usual, the natural frequencies are negative in the pedestal (due to strong edge electron diamagnetic rotation) and positive in the plasma core (due to strong core toroidal plasma rotation in the same direction as the toroidal plasma current). There is more shear in the natural frequency curve than is evident in Fig. 3, because discharge 139059 was not subject to rotation braking. Note that the natural frequency curve again passes though zero in the middle of the plasma, rather than at the top of the pedestal. We speculate that this is the case because diamagnetic contributions to the natural frequency scale as the inverse-square of plasma minor radius, and are, therefore, comparatively stronger in spherical tokamaks than in conventional aspect-ratio tokamaks.

E. $n = 1$ NTM stability

Five of the $n = 1$ tearing modes resonant in discharge 139057 are metastable to NTMs. As before, these modes are resonant in the middle of the plasma, close to the zero-crossing of the natural frequency curve. The unstable modes are the $m = 3$, with a natural frequency of -18.8 krad/s, the $m = 4$, with a natural frequency of 3.1 krad/s, the $m = 5$, a with natural frequency of 14.5 krad/s, the $m = 6$, with a natural frequency of 20.2 krad/s, and the $m = 7$, with a natural frequency of 23.9 krad/s. Figure 14 shows the right-hand sides of the modified Rutherford island width evolution equations for the $m = 3$, 4, 5, 6, and

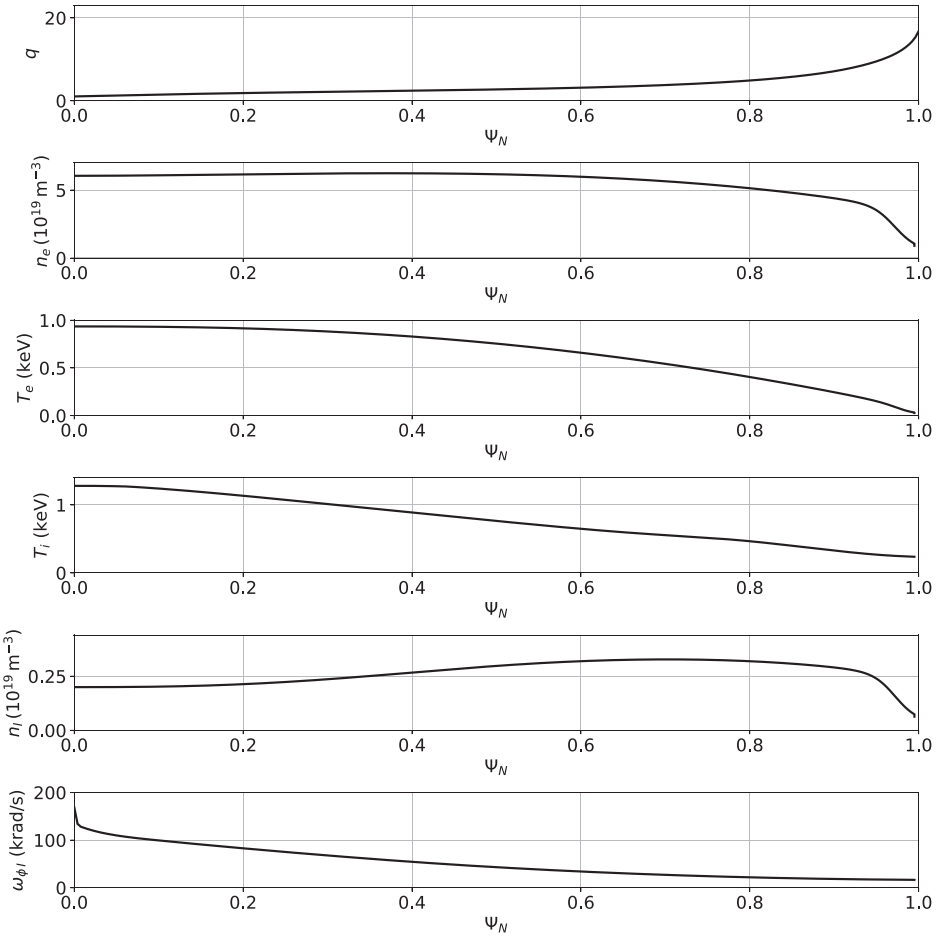

FIG. 12. Safety-factor, electron number density, electron temperature, impurity ion number density, and impurity ion toroidal rotation profiles in NSTX discharge 139057 at $t = 557$ ms.

7 modes as functions of island width. It can be seen that the most unstable mode is the $m = 3$, and that the $m = 7$ mode is only barely unstable (because its RHS barely crosses zero).

F. $n = 1$ RMP

As before, the $n = 1$ transient rotating RMP that is used to (theoretically) trigger $n = 1$ NTMs in discharge 139057 is generated by pulsing a rotating $n = 1$ current in the RMP coils installed on NSTX.

G. Pulse frequency scan

Figure 15 shows the critical $n = 1$ RMP current pulse amplitude required to trigger an NTM in discharge 139057 as a function of the pulse frequency for a pulse duration of 20 ms. The critical pulse amplitude exhibits a minimum value (which is not quite zero) when the pulse frequency matches the linear natural frequency of the $m = 3$ tearing mode. The critical pulse amplitude also exhibits secondary minima when the pulse frequency matches the linear natural frequencies of the $m = 4$, the $m = 5$, and the $m = 6$ tearing modes. Again, this is a synergistic effect by which the pulse simultaneously triggers both an $m = 3$ and an $m = 4$ NTM, or an $m = 3$, an $m = 4$, and an $m = 5$ NTM, etc. There is no clear secondary minimum when the pulse frequency matches the linear natural frequency of the $m = 7$ tearing mode, because the $m = 7$ NTM is comparatively feeble.

V. SUMMARY AND CONCLUSIONS

The EPEC asymptotic matching code has been used to simulate the triggering of $n = 1$ NTMs by a pulsed, rotating, $n = 1$ RMP in two example NSTX discharges. Although the two discharges are significantly different (the first is double-null, the second is single-null; the first is subject to $n = 3$ rotation braking, the second is not; the first has no fresh lithium coating on the plasma-facing wall-tiles, the second does), the results of the two sets of simulations are quite similar. The critical $n = 1$ RMP pulse amplitude required to trigger an $n = 1$ NTM is minimized when the RMP pulse rotation frequency matches the *linear* natural frequency of an $n = 1$ tearing mode, resonant within the plasma, that is metastable to an NTM. However, if there is a frequency mismatch, then the seed magnetic island chain driven at the relevant resonant surface is forced to rotate with respect to the RMP, because the RMP pulse amplitude is nowhere near sufficient to lock the island chain to the RMP. This rotation causes the critical RMP pulse amplitude required to trigger an NTM to oscillate as the RMP pulse duration is varied. The critical amplitude is minimized when the RMP pulse duration is such that seed island chain executes a half-integer

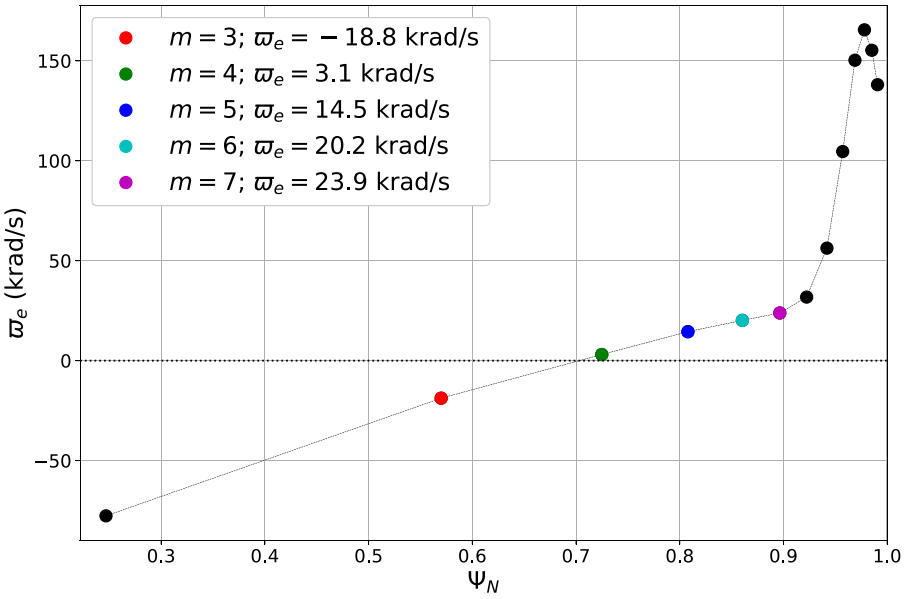

FIG. 13. Linear $n = 1$ natural frequencies in NSTX discharge 139057. There are 13 $n = 1$ resonant surfaces in the plasma corresponding to $m = 2$ through $m = 14$. Only the $m = 3$, 4, 5, 6, and 7 surfaces are potentially unstable to NTMs.

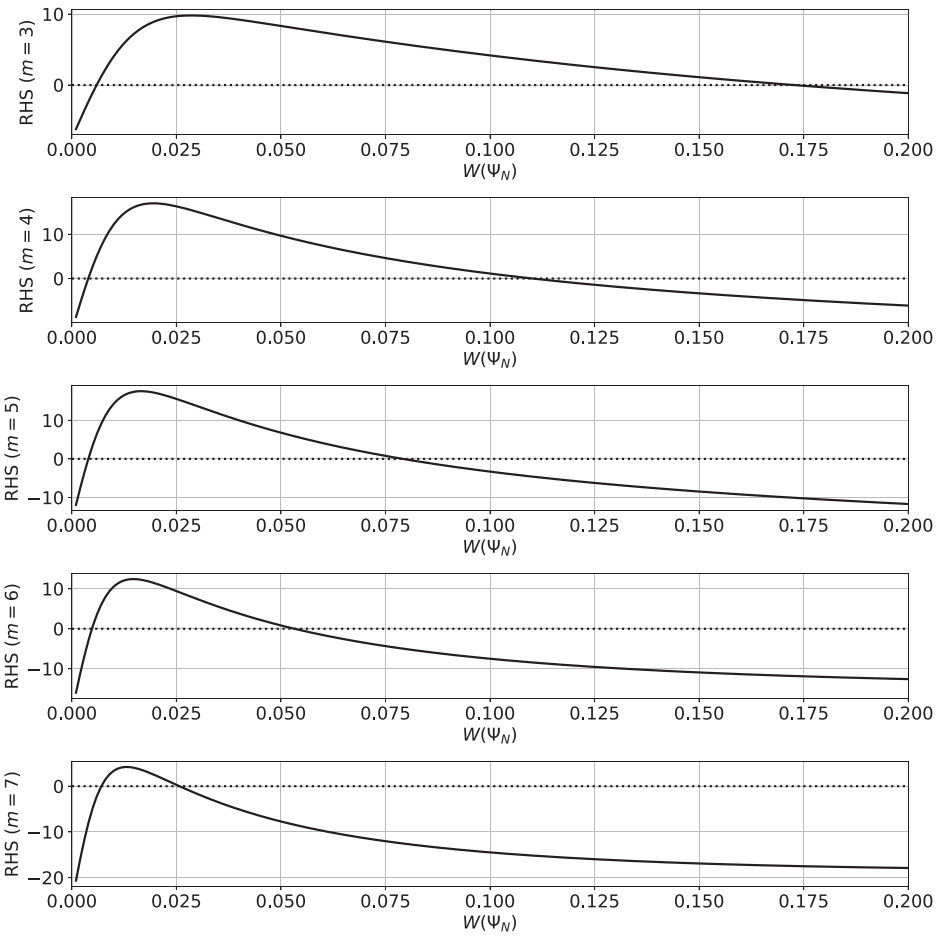

FIG. 14. Right-hand sides of the modified Rutherford equations for the $m = 3/n = 1$, 4/1, 5/1, 6/1, and 7/1 tearing modes in NSTX discharge 139057.

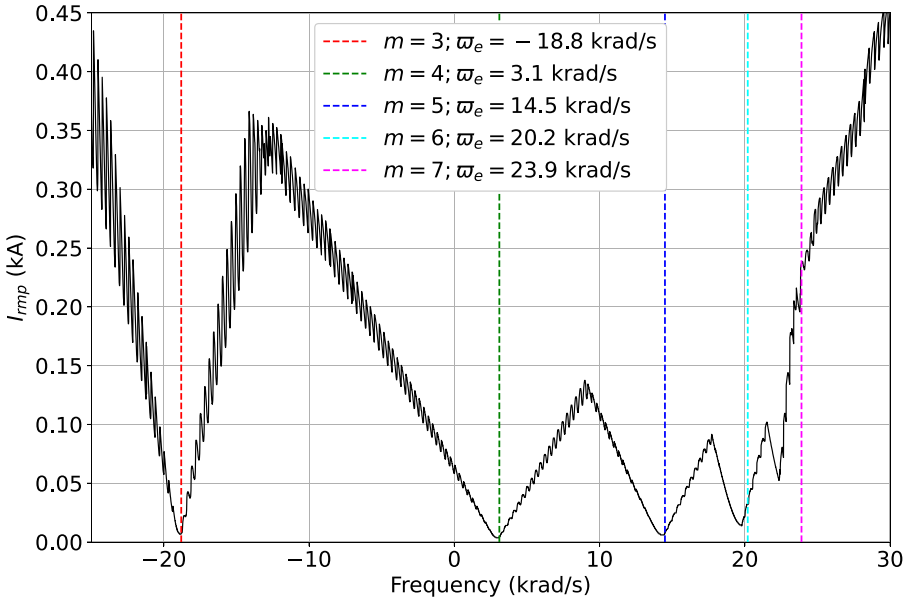

FIG. 15. Critical $n = 1$ RMP coil current pulse amplitude required to trigger an NTM in NSTX discharge 139057 as a function of the pulse frequency for a pulse duration of 20 ms.

number of rotations with respect to the pulse. All of the minima have the same value.

One of the most important insights gained in the study presented in this paper is that, although the triggering of an NTM by a transient, rotating, RMP is particularly easy when the frequency of the RMP matches the natural frequency of the NTM, triggering is still possible when there is a modest (e.g., 10 krad/s) frequency mismatch between the RMP and the NTM. Moreover, the rotation frequency of the seed island driven by the RMP does not generally match either the frequency of the RMP or the natural frequency of the NTM, but lies somewhere between these two frequencies.

ACKNOWLEDGMENTS

The authors would like to thank J. Canik for providing some of the NSTX data used in this paper. The authors would also like to thank N. C. Logan for his advice on how to run the GPEC code. Finally, the authors would like to thank S. Mordijck for helpful discussions. Part of the data analysis was performed using the OMFIT integrated modeling framework.[38]

This research was directly funded by the U.S. Department of Energy, Office of Science, Office of Fusion Energy Sciences, under Contract No. DE-SC0021156.

AUTHOR DECLARATIONS

Conflict of Interest

The authors have no conflicts to disclose.

Author Contributions

Richard Fitzpatrick: Conceptualization (equal); Formal analysis (equal); Funding acquisition (equal); Investigation (equal); Methodology (equal); Software (equal); Writing – original draft (equal); Writing – review & editing (equal). **Rajesh Maingi:** Data curation (equal); Writing – review & editing (supporting). **Jong-Kyu Park:** Software (supporting); Writing – review & editing (supporting). **S.A. Sabbagh:** Writing – review & editing (supporting).

DATA AVAILABILITY

The digital data used in the figures in this paper can be obtained from the corresponding author upon reasonable request.

APPENDIX: DESCRIPTION OF EPEC MODEL

1. Introduction

The (extended perturbed equilibrium code) EPEC model was introduced in Ref. 10, and improved in Refs. 11–13. The model has been further extended for the study presented in this paper. The latest improvements to the model include the introduction of perturbed bootstrap current, magnetic field-line curvature, ion polarization current, and island saturation terms into the resonant plasma response model (see subsections 2 e, 3 e, 3 f, and 4 d of the Appendix); a more accurate calculation of the critical island widths needed to locally flatten the electron temperature, the ion temperature, and the electron number density profiles (see subsection 4 c of the Appendix); and a better calculation of the natural frequencies of tearing modes (see subsection 5 b of the Appendix). Finally, we have corrected a previous error in Eqs. (A38), (A39), (A44), (A45), (A47), and (A48).

2. Plasma response in outer region

a. Coordinates

Let R, ϕ, and Z be right-handed cylindrical coordinates whose symmetry axis corresponds to the toroidal symmetry axis of the plasma. Let r, θ, and ϕ be right-handed flux coordinates whose Jacobian is $\mathcal{J} \equiv (\nabla r \times \nabla\theta \cdot \nabla\phi)^{-1} = r R^2/R_0$. Here, R_0 is a convenient scale major radius, r is a magnetic flux-surface label with

dimensions of length, and θ is an axisymmetric angular coordinate that increases by 2π radians for every poloidal circuit of the magnetic axis. Let $r=0$ correspond to the magnetic axis, and let $r = r_{100}$ correspond to the last closed magnetic flux-surface.

b. Equilibrium magnetic field

The equilibrium magnetic field is written $\mathbf{B} = R_0\, B_0[f(r)\,\nabla\phi \times\nabla r + g(r)\,\nabla\phi]$, where B_0 is a convenient scale toroidal magnetic field-strength, and $q(r) = r\,g/(R_0 f)$ is the safety-factor profile.[10] The equilibrium poloidal magnetic flux, $\Psi_p(r)$, satisfies $d\Psi_p/dr = R_0\, B_0 f(r)$, where, by convention, $\Psi_p(r_{100}) = 0$. The normalized poloidal magnetic flux, $\Psi_N(r)$, is defined such that $\Psi_N(r) = 1 - \Psi_p(r)/\Psi_p(0)$. Hence, $\Psi_N(0) = 0$ and $\Psi_N(r_{100}) = 1$.

c. Perturbed magnetic field

Consider the response of the plasma to an RMP with $n>0$ periods in the toroidal direction. We can write the components of the perturbed magnetic field in the form[10]

$$\frac{r\,R^2\,\delta\mathbf{B}\cdot\nabla r}{R_0^2} = \mathrm{i}\sum_j \psi_j(r)\,\mathrm{e}^{\,\mathrm{i}\,(m_j\theta - n\,\phi)}, \tag{A1}$$

$$R^2\,\delta\mathbf{B}\cdot\nabla\phi = n\sum_j \frac{\Xi_j(r)}{m_j}\,\mathrm{e}^{\,\mathrm{i}\,(m_j\,\theta - n\,\phi)}, \tag{A2}$$

where the sum is over all relevant poloidal harmonics of the perturbed magnetic field.

Let there be K resonant (i.e., rational) magnetic flux-surfaces in the plasma, labeled 1 through K. Consider the kth resonant surface, $r=r_k$, at which $q(r_k) = m_k/n$, where m_k is a positive integer. Let $\Psi_k = \psi_k(r_k)/m_k$, and $\Delta\Psi_k = [\Xi_k]_{r_{k-}}^{r_{k+}}$. Here, Ψ_k is the (complex) reconnected helical magnetic flux at the kth resonant surface, whereas $\Delta\Psi_k$ is a (complex) measure of the strength of the current sheet at the same resonant surface.

d. Toroidal tearing mode dispersion relation

In the presence of the RMP, the Ψ_k and the $\Delta\Psi_k$ values are related according to the inhomogeneous toroidal tearing mode dispersion relation, which takes the form[10,20]

$$\Delta\Psi_k = \sum_{k'=1,K} E_{kk'}\,\Psi_{k'} + |E_{kk}|\,\chi_k. \tag{A3}$$

Here, $E_{kk'}$ (for k, $k' = 1$, K) is the dimensionless, Hermitian, toroidal tearing mode stability matrix,[20] whereas the χ_k (for $k = 1, K$) parameterize the current sheets driven at the various resonant surfaces when the plasma responds to the applied RMP in accordance with the equations of linearized, marginally stable, ideal-MHD.

The EPEC model determines the elements of the $E_{kk'}$ matrix using a high-q approximation. In fact, if $F_{kk'}$ is the inverse of the $E_{kk'}$ matrix, then[10]

$$F_{kk'} = \oint\!\!\oint G(R_k, Z_k; R_{k'}, Z_{k'})\,\mathrm{e}^{-\mathrm{i}\,(m_k\,\theta_k - m_{k'}\,\theta_{k'})}\,\frac{d\theta_k}{2\pi}\,\frac{d\theta_{k'}}{2\pi} \tag{A4}$$

and

$$G(R_k, Z_k; R_{k'}, Z_{k'}) = \frac{(-1)^n\,\pi^2\,R_k\,R_{k'}/R_0}{2\,\Gamma(1/2)\,\Gamma(n+1/2)}\left[\frac{\cosh\eta_{kk'}}{R_k^2 + R_{k'}^2 + (Z_k - Z_{k'})^2}\right]^{1/2} \times\left[(n-1/2)\,P_{-1/2}^{n-1}(\cosh\eta_{kk'}) + \frac{P_{-1/2}^{n+1}(\cosh\eta_{kk'})}{n+1/2}\right] \tag{A5}$$

with

$$\eta_{kk'} = \tanh^{-1}\left[\frac{2\,R_k\,R_{k'}}{R_k^2 + R_{k'}^2 + (Z_k - Z_{k'})^2}\right]. \tag{A6}$$

Here, the double integral in Eq. (A4) is taken around the kth resonant surface and the k' th resonant surface. Finally, the $\Gamma(z)$ and $P_\mu^\nu(z)$ are gamma functions and associated Legendre functions, respectively.

The (complex) χ_k parameters are determined from the GPEC code.[36] To be more exact, the GPEC code calculates the (complex) dimensionless $\Delta_{m_k n}$ parameters, which measure the strengths of the ideal current sheets that develop at the various resonant magnetic flux-surfaces in the plasma in response to the applied RMP. The $\Delta_{m_k n}$ parameters are related to the χ_k parameters according to

$$\frac{\chi_k}{R_0\,B_0} = -\mathrm{i}\,\frac{\Delta_{m_k n}}{|E_{kk}|}\left(\frac{r_k}{R_0}\right)^2\frac{g(r_k)}{m_k\left[a_{kk}(r_k) + (r_k/R_0\,q_k)^2\right]}, \tag{A7}$$

where $q_k = m_k/n$, and $a_{kk}(r) = \oint |\nabla r|^{-2}\,d\theta/(2\pi)$.

e. Glasser–Greene–Johnson parameters

Let $\hat{B} = |\mathbf{B}|/B_0$, $\hat{\nabla} = R_0\,\nabla$, and $d\psi_p/dr = f(r)/R_0$. The angle Θ and the parameter γ are defined in subsection 3 b of the Appendix. Let

$$J_1(r) = \oint\frac{1}{\hat{B}}\,\frac{d\Theta}{2\pi}, \tag{A8}$$

$$J_2(r) = \oint\hat{B}\,\frac{d\Theta}{2\pi}, \tag{A9}$$

$$J_3(r) = \oint\frac{1}{\hat{B}^3}\,\frac{d\Theta}{2\pi}, \tag{A10}$$

$$J_4(r) = \oint\frac{1}{\hat{B}\,|\hat{\nabla}\psi_p|^2}\,\frac{d\Theta}{2\pi}, \tag{A11}$$

$$J_5(r) = \oint\frac{\hat{B}}{|\hat{\nabla}\psi_p|^2}\,\frac{d\Theta}{2\pi}, \tag{A12}$$

$$J_6(r) = \oint\frac{1}{\hat{B}^3|\hat{\nabla}\psi_p|^2}\,\frac{d\Theta}{2\pi}. \tag{A13}$$

It follows that[39]

$$E(r) = -\frac{dP/d\psi_p}{(dq/d\psi_p)^2}\,\frac{1}{\gamma}\left[\frac{d}{d\psi_p}\left(\frac{J_1}{\gamma}\right) - g\,\frac{dq}{d\psi_p}\,\frac{J_1}{J_2}\right]J_5, \tag{A14}$$

$$F(r) = \frac{(dP/d\psi_p)^2}{(dq/d\psi_p)^2}\,\frac{1}{\gamma^2}\left[g^2\left(J_5\,J_6 - J_4^2\right) + J_5\,J_3\right], \tag{A15}$$

$$H(r) = \frac{dP/d\psi_p}{dq/d\psi_p}\frac{g}{\gamma}\left(J_4 - \frac{J_1 J_5}{J_2}\right), \tag{A16}$$

where $P(r)$ is the total plasma pressure. Finally,

$$D_R(r) = E + F + H^2. \tag{A17}$$

f. Current gradient parameters

The normalized toroidal plasma current density profile is written as

$$\hat{J}_\phi(r) = -\frac{\mu_0 R_0 R}{B_0}\frac{dP}{d\Psi_p} - R_0^2 B_0 g \frac{dg}{d\Psi_p}. \tag{A18}$$

The previous expression is evaluated on the outboard mid-plane. Let $\hat{J}'_\phi = d\hat{J}_\phi/dr$, $\hat{J}''_\phi = d^2\hat{J}_\phi/dr^2$, $s(r) = d\ln q/d\ln r$, $A_k = -(r\,q\,\hat{J}'_\phi/s)_{r_k}$, and $B_k = -(r^2\,q\,\hat{J}''_\phi/s)_{r_k}$.

3. Neoclassical model

a. Plasma species

The plasma is assumed to consist of three (charged) species: electrons (e), majority ions (i), and impurity ions (I). The charges of the three species are $e_e = -e$, $e_i = e$, and $e_I = Z_I\,e$, respectively, where e is the magnitude of the electron charge. Quasi-neutrality demands that $n_e = n_i + Z_I\,n_I$, where $n_a(r)$ is the species-a number density. Let $\alpha_I(r) = Z_I\,(Z_{\rm eff} - 1)/(Z_I - Z_{\rm eff})$, where $Z_{\rm eff}(r) = (n_i + Z_I^2\,n_I)/n_e$ is the effective ion charge number. It follows that $n_i/n_e = (Z_I - Z_{\rm eff})/(Z_I - 1)$ and $n_I/n_e = (Z_{\rm eff} - 1)/[Z_I\,(Z_I - 1)]$. Finally, let $Z_{{\rm eff}\,i} = (Z_I - Z_{\rm eff})/(Z_I - 1)$ and $Z_{{\rm eff}\,I} = Z_I\,(Z_{\rm eff} - 1)/(Z_I - 1)$.

b. Collisionality parameters

Consider an equilibrium magnetic flux-surface whose label is r. Let[25]

$$\frac{1}{\gamma(r)} = \frac{q}{g}\oint\frac{B\,R^2}{B_0\,R_0^2}\frac{d\theta}{2\pi}. \tag{A19}$$

It is helpful to define a new poloidal angle Θ such that

$$\frac{d\Theta}{d\theta} = \frac{\gamma\,q}{g}\frac{B\,R^2}{B_0\,R_0^2}. \tag{A20}$$

Let

$$I_1 = \oint\frac{B_0}{B}\frac{d\Theta}{2\pi}, \tag{A21}$$

$$I_2 = \oint\frac{B}{B_0}\frac{d\Theta}{2\pi}, \tag{A22}$$

$$I_3 = \oint\left(\frac{\partial B}{\partial\Theta}\right)^2\frac{1}{B_0\,B}\frac{d\Theta}{2\pi}, \tag{A23}$$

$$I_{4,j} = \sqrt{2}\,j\oint\frac{\cos(j\,\Theta)}{B/B_0}\frac{d\Theta}{2\pi}, \tag{A24}$$

$$I_{5,j} = \sqrt{2}\,j\oint\frac{\cos(j\,\Theta)}{2\,(B/B_0)^2}\frac{d\Theta}{2\pi}, \tag{A25}$$

$$I_6(\lambda) = \oint\frac{\sqrt{1 - \lambda\,B/B_{\rm max}}}{B/B_0}\frac{d\Theta}{2\pi}, \tag{A26}$$

where $B_{\rm max}$ is the maximum value of B on the magnetic flux-surface, and j is a positive integer. The species-a transit frequency is written as $\omega_{t\,a}(r) = K_t\,\gamma\,v_{T\,a}$, where

$$K_t(r) = \frac{I_1^2\,I_3}{I_2^2\sum_{j=1,\infty} I_{4,j}\,I_{5,j}}, \tag{A27}$$

and $v_{T\,a} = \sqrt{2\,T_a/m_a}$. Here, m_a is the species-a mass, and $T_a(r)$ is the species-a temperature (in energy units). The fraction of circulating particles is

$$f_c(r) = \frac{3\,I_2}{4}\frac{B_0^2}{B_{\rm max}^2}\int_0^1\frac{\lambda\,d\lambda}{I_6(\lambda)}. \tag{A28}$$

Finally, the dimensionless species-a collisionality parameter is written as $\nu_{*\,a}(r) = K_*\,g_t/(\omega_{t\,a}\,\tau_{aa})$, where $g_t(r) = (1 - f_c)/f_c$,

$$K_*(r) = \frac{3}{8\pi}\frac{I_2}{I_3}K_t^2 \tag{A29}$$

$$\frac{1}{\tau_{aa}(r)} = \frac{4}{3\sqrt{\pi}}\frac{4\pi\,n_a\,e_a^4\,\ln\Lambda}{(4\pi\,\epsilon_0)^2\,m_a^2\,v_{T\,a}^3}. \tag{A30}$$

Here, the Coulomb logarithm, $\ln\Lambda$, is assumed to take the same large constant value (i.e., $\ln\Lambda \simeq 17$), independent of species.

c. Collisional friction matrices

Let $x_{ab} = v_{T\,b}/v_{T\,a}$. The 2×2 dimensionless ion collisional friction matrices, $[F^{ii}](r)$, $[F^{iI}](r)$, $[F^{Ii}](r)$, and $[F^{II}](r)$, are defined to have the following elements:[25]

$$F_{00}^{ii} = \frac{\alpha_I\,(1 + m_i/m_I)}{(1 + x_{iI}^2)^{3/2}}, \tag{A31}$$

$$F_{01}^{ii} = \frac{3}{2}\frac{\alpha_I\,(1 + m_i/m_I)}{(1 + x_{iI}^2)^{5/2}}, \tag{A32}$$

$$F_{11}^{ii} = \sqrt{2} + \frac{\alpha_I\left[13/4 + 4\,x_{iI}^2 + (15/2)\,x_{iI}^4\right]}{(1 + x_{iI}^2)^{5/2}}, \tag{A33}$$

$$F_{01}^{iI} = \frac{3}{2}\frac{T_i}{T_I}\frac{\alpha_I\,(1 + m_I/m_i)}{x_{iI}\,(1 + x_{Ii}^2)^{5/2}}, \tag{A34}$$

$$F_{11}^{iI} = \frac{27}{4}\frac{T_i}{T_I}\frac{\alpha_I\,x_{iI}^2}{(1 + x_{iI}^2)^{5/2}}, \tag{A35}$$

$$F_{11}^{Ii} = \frac{27}{4}\frac{\alpha_I\,x_{iI}^2}{(1 + x_{iI}^2)^{5/2}}, \tag{A36}$$

$$F_{11}^{II} = \frac{T_i}{T_I}\left\{\sqrt{2}\,\alpha_I^2\,x_{Ii} + \frac{\alpha_I\left[15/2 + 4\,x_{iI}^2 + (13/4)\,x_{iI}^4\right]}{(1 + x_{iI}^2)^{5/2}}\right\}, \tag{A37}$$

$$F_{10}^{ii} = F_{01}^{ii},\quad F_{00}^{iI} = F_{00}^{ii},\quad F_{10}^{iI} = F_{01}^{ii},\quad F_{00}^{Ii} = F_{00}^{ii},\quad F_{01}^{Ii} = F_{01}^{ii},$$
$$F_{10}^{Ii} = F_{01}^{iI},\quad F_{00}^{II} = F_{00}^{ii},\quad F_{01}^{II} = F_{01}^{iI},\quad F_{10}^{II} = F_{01}^{iI}.$$

The 2×2 dimensionless electron collisional friction matrices, $[F^{ee}](r)$, $[F^{ei}](r)$, and $[F^{eI}](r)$, are defined to have the following elements:[25] $F^{ee}_{00}=Z_{\rm eff}$, $F^{ee}_{01}=(3/2)\,Z_{\rm eff}$, $F^{ee}_{10}=F^{ee}_{01}$, $F^{ee}_{11}=\sqrt{2}+(13/4)\,Z_{\rm eff}$, $F^{ei}_{00}=Z_{{\rm eff}\,i}$, $F^{ei}_{01}=F^{ei}_{11}=0$, $F^{ei}_{10}=(3/2)\,Z_{{\rm eff}\,i}$, $F^{eI}_{00}=Z_{{\rm eff}\,I}$, $F^{eI}_{01}=F^{eI}_{11}=0$, $F^{eI}_{10}=(3/2)\,Z_{{\rm eff}\,I}$.

d. Neoclassical viscosity matrices

The 2×2 dimensionless species-a neoclassical viscosity matrix, $[\mu^a](r)$, is defined to have the following elements:[25] $\mu^a_{00}=K^a_{00}$, $\mu^a_{01}=(5/2)\,K^a_{00}-K^a_{01}$, $\mu^a_{10}=\mu^a_{01}$, $\mu^a_{11}=K^a_{11}-5\,K^a_{01}+(25/4)\,K^a_{00}$. Here,

$$K^e_{jk}=g_t\,\frac{8}{3\sqrt{\pi}}\int_0^\infty\frac{e^{-x^2}\,x^{9+2\,(j+k)}\,\nu^e_D(x)\,dx}{\left[x^4+\nu_{*e}\,\nu^e_D(x)\right]\left[x^4+(5\pi/8)\,(\omega_{te}\,\tau_{ee})^{-1}\,\nu^e_T(x)\right]},\tag{A38}$$

$$\nu^e_D=\frac{3\sqrt{\pi}}{4}\left[\left(1-\frac{1}{2\,x^2}\right)\psi(x)+\psi'(x)\right]+\frac{3\sqrt{\pi}}{4}\,Z_{\rm eff},\tag{A39}$$

$$\nu^e_\epsilon=\frac{3\sqrt{\pi}}{2}\left[\psi(x)-\psi'(x)\right],\tag{A40}$$

$$\nu^a_T(x)=3\,\nu^a_D(x)+\nu^a_\epsilon(x),\tag{A41}$$

and

$$\psi(x)=\frac{2}{\sqrt{\pi}}\int_0^x e^{-t^2}\,dt-\frac{2}{\sqrt{\pi}}\,x\,e^{-x^2},\tag{A42}$$

$$\psi'(x)=\frac{2}{\sqrt{\pi}}\,x\,e^{-x^2}.\tag{A43}$$

Furthermore,

$$K^i_{jk}=g_t\,\frac{8}{3\sqrt{\pi}}\int_0^\infty\frac{e^{-x^2}\,x^{8+2\,(j+k)}\,\nu^i_D(x)\,dx}{\left[x^3+\nu_{*i}\,\nu^i_D(x)\right]\left[x^3+(5\pi/8)\,(\omega_{ti}\,\tau_{ii})^{-1}\,\nu^i_T(x)\right]},\tag{A44}$$

$$\nu^i_D=\frac{3\sqrt{\pi}}{4}\left[\left(1-\frac{1}{2\,x^2}\right)\psi(x)+\psi'(x)\right]\frac{1}{x}+\frac{3\sqrt{\pi}}{4}\,\alpha_I\left[\left(1-\frac{x^2_{iI}}{2\,x^2}\right)\psi\left(\frac{x}{x_{iI}}\right)+\psi'\left(\frac{x}{x_{iI}}\right)\right]\frac{1}{x},\tag{A45}$$

$$\nu^i_\epsilon=\frac{3\sqrt{\pi}}{2}\left[\psi(x)-\psi'(x)\right]\frac{1}{x}+\frac{3\sqrt{\pi}}{2}\,\alpha_I\left[\frac{m_i}{m_I}\,\psi\left(\frac{x}{x_{iI}}\right)-\psi'\left(\frac{x}{x_{iI}}\right)\right]\frac{1}{x},\tag{A46}$$

and, finally,

$$K^I_{jk}=g_t\,\frac{8}{3\sqrt{\pi}}\int_0^\infty\frac{e^{-x^2}\,x^{8+2\,(j+k)}\,\nu^I_D(x)\,dx}{\left[x^3+\nu_{*I}\,\nu^I_D(x)\right]\left[x^3+(5\pi/8)\,(\omega_{tI}\,\tau_{II})^{-1}\,\nu^I_T(x)\right]},\tag{A47}$$

$$\nu^I_D=\frac{3\sqrt{\pi}}{4}\left[\left(1-\frac{1}{2\,x^2}\right)\psi(x)+\psi'(x)\right]\frac{1}{x}+\frac{3\sqrt{\pi}}{4}\,\frac{1}{\alpha_I}\left[\left(1-\frac{x^2_{Ii}}{2\,x^2}\right)\psi\left(\frac{x}{x_{Ii}}\right)+\psi'\left(\frac{x}{x_{Ii}}\right)\right]\frac{1}{x},\tag{A48}$$

$$\nu^I_\epsilon=\frac{3\sqrt{\pi}}{2}\left[\psi(x)-\psi'(x)\right]\frac{1}{x}+\frac{3\sqrt{\pi}}{2}\,\frac{1}{\alpha_I}\left[\frac{m_I}{m_i}\,\psi\left(\frac{x}{x_{Ii}}\right)-\psi'\left(\frac{x}{x_{Ii}}\right)\right]\frac{1}{x}.\tag{A49}$$

e. Parallel force and heat balance

Let $[\tilde\mu^I]=\alpha_I^2\,(T_i/T_I)\,x_{Ii}\,[\mu^I]$. The requirement of equilibrium force and heat balance parallel to the magnetic field leads us to define four 2×2 dimensionless ion matrices, $[L^{ii}](r)$, $[L^{iI}](r)$, $[L^{Ii}](r)$, and $[L^{II}](r)$, where[25]

$$\begin{pmatrix}[L^{ii}], & [L^{iI}]\\ [L^{Ii}], & [L^{II}]\end{pmatrix}=\begin{pmatrix}\left[F^{ii}+\mu^i+Y^{in}/y_n\right], & -[F^{iI}]\\ -[F^{Ii}], & \left[F^{II}+\tilde\mu^I\right]\end{pmatrix}^{-1}\times\begin{pmatrix}[F^{ii}+Y^{in}], & -[F^{iI}]\\ -[F^{Ii}], & [F^{II}]\end{pmatrix},\tag{A50}$$

and the additional four 2×2 dimensionless ion matrices, $[G^{ii}](r)$, $[G^{iI}](r)$, $[G^{Ii}](r)$, and $[G^{II}](r)$, where

$$\begin{pmatrix}[G^{ii}], & [G^{iI}]\\ [G^{Ii}], & [G^{II}]\end{pmatrix}=\tau_{ii}\,\langle\sigma\,v\rangle^{cx}_i\,\langle n_n\rangle\times\begin{pmatrix}\left[F^{ii}+\mu^i+Y^{in}/y_n\right], & -[F^{iI}]\\ -[F^{Ii}], & \left[F^{II}+\tilde\mu^I\right]\end{pmatrix}^{-1},\tag{A51}$$

and the 2×2 dimensionless electron matrices, $[Q^{ee}](r)$, $[G^{ei}](r)$, $[L^{ee}](r)$, $[L^{ei}](r)$, and $[L^{eI}](r)$, where

$$[Q^{ee}]=\left[F^{ee}+\mu^e\right]^{-1},\tag{A52}$$

$$[G^{ei}]=[Q^{ee}]\left([F^{ei}]\,[G^{ii}]+[F^{eI}]\,[G^{Ii}]\right),\tag{A53}$$

$$[L^{ee}]=[Q^{ee}]\,[F^{ee}],\tag{A54}$$

$$[L^{ei}]=[Q^{ee}]\left\{[F^{ei}]\,[L^{ii}]-[F^{ei}]+[F^{eI}]\,[L^{Ii}]\right\},\tag{A55}$$

$$[L^{eI}]=[Q^{ee}]\left\{[F^{eI}]\,[L^{II}]-[F^{eI}]+[F^{ei}]\,[L^{iI}]\right\}.\tag{A56}$$

Here,[40]

$$[Y^{in}]=\tau_{ii}\,\langle\sigma\,v\rangle^{cx}_i\,\langle n_n\rangle\begin{bmatrix}1, & 0\\ 0, & E_n/T_i\end{bmatrix},\tag{A57}$$

$$y_n=\frac{\langle n_n\rangle\,\langle B^2\rangle}{\langle n_n\,B^2\rangle},\tag{A58}$$

where

$$\langle A\rangle(r)\equiv\oint\frac{A(r,\Theta)\,d\Theta}{B(r,\Theta)}\Big/\oint\frac{d\Theta}{B(r,\Theta)}.\tag{A59}$$

Moreover, $\langle\sigma\,v\rangle^{cx}_i$ is the flux-surface averaged rate constant for charge-exchange reactions between neutrals and majority ions, $n_n(r,\Theta)$ is the neutral particle number density, and E_n/T_i is the ratio of the incoming neutral energy to the majority ion energy. The parameter y_n takes into account the fact that the incoming neutrals at the edge of an H-mode tokamak plasma are usually concentrated at the X-point (i.e., $y_n>1$).

f. Neoclassical frequencies

The neoclassical frequencies of the three plasma species have the following definitions:

$$\omega_{\mathrm{nc}\,i}(r) = -G_{00}^{ii}\,\omega_E - \left[L_{00}^{ii} - L_{01}^{ii}\left(\frac{\eta_i}{1+\eta_i}\right)\right]\omega_{*\,i} - \left[L_{00}^{iI} - L_{01}^{iI}\left(\frac{\eta_I}{1+\eta_I}\right)\right]\omega_{*\,I}, \tag{A60}$$

$$\omega_{\mathrm{nc}\,I}(r) = -G_{00}^{Ii}\,\omega_E - \left[L_{00}^{II} - L_{01}^{II}\left(\frac{\eta_I}{1+\eta_I}\right)\right]\omega_{*\,I} - \left[L_{00}^{Ii} - L_{01}^{Ii}\left(\frac{\eta_i}{1+\eta_i}\right)\right]\omega_{*\,i}, \tag{A61}$$

$$\omega_{\mathrm{nc}\,e}(r) = -G_{00}^{ei}\,\omega_E - \left[L_{00}^{ee} - L_{01}^{ee}\left(\frac{\eta_e}{1+\eta_e}\right)\right]\omega_{*\,e} - \left[L_{00}^{ei} - L_{01}^{ei}\left(\frac{\eta_i}{1+\eta_i}\right)\right]\omega_{*\,i} - \left[L_{00}^{eI} - L_{01}^{eI}\left(\frac{\eta_I}{1+\eta_I}\right)\right]\omega_{*\,I}. \tag{A62}$$

Here,

$$\omega_E(r) = -\frac{d\Phi}{d\Psi_p}, \tag{A63}$$

$$\omega_{*\,a}(r) = -\frac{T_a}{e_a}\frac{d\ln p_a}{d\Psi_p}, \tag{A64}$$

$$\eta_a(r) = \frac{d\ln T_a}{d\ln n_a}. \tag{A65}$$

Moreover, $p_a(r) = n_a\,T_a$, and $\Phi(r)$ is the equilibrium electric scalar potential.

g. Impurity ion angular rotation velocities

Let

$$\omega_{\theta\,I}(r) = \frac{\mathbf{V}^I\cdot\nabla\theta}{\mathbf{B}\cdot\nabla\theta}\frac{R_0\,B_0\,g}{R^2}, \tag{A66}$$

$$\omega_{\phi\,I}(r) = \mathbf{V}^I\cdot\nabla\phi, \tag{A67}$$

where $\mathbf{V}^I$ is the impurity ion fluid velocity, and the right-hand sides are evaluated on the outboard mid-plane. According to neoclassical theory,[13]

$$\omega_{\theta\,I} = K_\theta\,\omega_{\mathrm{nc}\,I}, \tag{A68}$$

$$\omega_{\phi\,I} = \omega_E + \omega_{*\,I} + \omega_{\theta\,I}, \tag{A69}$$

where

$$K_\theta(r) = \frac{R_0^2\,B_0^2\,g^2}{R^2\,\langle B^2\rangle}. \tag{A70}$$

4. Plasma response in inner region

a. Linear layer widths

Let

$$\tau_R(r) = \mu_0\,r^2\,\sigma_{ee}\,Q_{00}^{ee}, \tag{A71}$$

$$\sigma_{ee}(r) = \frac{n_e\,e^2\,\tau_{ee}}{m_e}, \tag{A72}$$

$$\tau_H(r) = \frac{R_0}{B_0\,g}\frac{\sqrt{\mu_0\,\rho}}{n\,s}, \tag{A73}$$

$$\rho(r) = m_i\,n_i(r) + m_I\,n_I(r), \tag{A74}$$

$$\tau_\perp(r) = \frac{r^2}{D_\perp}, \tag{A75}$$

$$\tau_\varphi(r) = \frac{r^2}{\chi_\phi}, \tag{A76}$$

$$\tau(r) = -\frac{\omega_{*\,e}}{\omega_{*\,i}}, \tag{A77}$$

$$d_\beta(r) = \frac{\sqrt{(5/3)\,m_i\,[T_e + (n_i/n_e)\,T_i + (n_I/n_e)\,T_I]}}{e\,B_0\,g}, \tag{A78}$$

$$S(r) = \frac{\tau_R}{\tau_H}, \tag{A79}$$

$$P_\varphi(r) = \frac{\tau_R}{\tau_\varphi}, \tag{A80}$$

$$P_\perp(r) = \frac{\tau_R}{\tau_\perp}, \tag{A81}$$

$$D(r) = S^{1/3}\left(\frac{\tau}{1+\tau}\right)^{1/2}\frac{d_\beta}{r}, \tag{A82}$$

$$Q_E(r) = -S^{1/3}\,n\,\omega_E\,\tau_H, \tag{A83}$$

$$Q_{e,i}(r) = -S^{1/3}\,n\,\omega_{*\,e,i}\,\tau_H. \tag{A84}$$

Here, $\chi_e(r)$, $D_\perp(r)$, and $\chi_\phi(r)$ are the perpendicular electron energy, particle, and toroidal momentum diffusivity profiles, respectively. The constant-ψ linear layer width is determined from the solution of[26,27]

$$\frac{d^2Y}{dp^2} - \left[\frac{-Q_E(Q_E+Q_i) + \mathrm{i}(Q_E+Q_i)(P_\varphi+P_\perp)p^2 + P_\varphi P_\perp p^4}{\mathrm{i}(Q_E+Q_e) + \{P_\perp + \mathrm{i}(Q_E+Q_i)D^2\}p^2 + (1+1/\tau)P_\varphi D^2 p^4}\right] \times p^2\,Y = 0. \tag{A85}$$

If the small-p behavior of the solution of the previous equation that is well-behaved as $p\to\infty$ is, then

$$Y(p) = Y_0\left[1 - c\,p + \mathcal{O}(p^2)\right]. \tag{A86}$$

Then, the linear layer width is

$$\delta_{\mathrm{linear}}(r) = \frac{\pi\,|c|\,r}{S^{1/3}}. \tag{A87}$$

Note that Eq. (A85) can only be solved when $1 + 1/\tau > 0$.

b. Island widths

Let $\Psi_k = R_0\,B_0\,\hat{\Psi}_k\,\mathrm{e}^{-\mathrm{i}\,\varphi_k}$, where $\hat{\Psi}_k > 0$ and φ_k are both real quantities. The full width (in r) of the magnetic island chain at the kth resonant surface is[10]

$$W_k = 4\,R_0\left(\frac{q}{g\,s}\right)^{1/2}_{r_k}\hat{\Psi}_k^{\,1/2}. \tag{A88}$$

c. Critical island widths

The critical full island width (in r), which must be exceeded before the electron temperature is flattened within the magnetic separatrix of the magnetic island chain at the kth resonant surface, is[7,41]

$$W_{T_e k} = \sqrt{8}\left(\frac{\chi_e}{\chi_{\parallel e}}\right)_{r_k}^{1/4}\left(\frac{1}{\epsilon\, s\, n}\right)_{r_k}^{1/2} r_k, \tag{A89}$$

where $\epsilon = r/R_0$, and

$$\chi_{\parallel e} = \frac{\chi_{\parallel e}^{\text{brag}}\,\chi_{\parallel e}^{\max}}{\chi_{\parallel e}^{\text{brag}} + \chi_{\parallel e}^{\max}}, \tag{A90}$$

$$\chi_{\parallel e}^{\text{brag}} = \frac{1.581\,\tau_{ee}\,v_{Te}^2}{1 + 0.2535\,Z_{\text{eff}}}, \tag{A91}$$

$$\chi_{\parallel e}^{\max} = \frac{2\,R_0\,v_{Te}}{\pi^{1/2}\,n\,s}\,\frac{r_k}{W_{T_e k}}. \tag{A92}$$

Equations (A89)–(A92) must be solved iteratively for $W_{T_e k}/r_k$.

The critical full island width (in r), which must be exceeded before the ion temperature is flattened within the magnetic separatrix of the magnetic island chain at the kth resonant surface, is[7,41]

$$W_{T_i k} = \sqrt{8}\left(\frac{\chi_i}{\chi_{\parallel i}}\right)_{r_k}^{1/4}\left(\frac{1}{\epsilon\, s\, n}\right)_{r_k}^{1/2} r_k, \tag{A93}$$

where $\chi_i(r)$ is the perpendicular ion energy diffusivity profile,

$$\chi_{\parallel i} = \frac{\chi_{\parallel i}^{\text{brag}}\,\chi_{\parallel i}^{\max}}{\chi_{\parallel i}^{\text{brag}} + \chi_{\parallel i}^{\max}}, \tag{A94}$$

$$\chi_{\parallel i}^{\text{brag}} = \frac{1.953\,\tau_{ii}\,v_{Ti}^2}{\sqrt{2}\,Z_{\text{eff}}}, \tag{A95}$$

$$\chi_{\parallel i}^{\max} = \frac{2\,R_0\,v_{Ti}}{\pi^{1/2}\,n\,s}\,\frac{r_k}{W_{T_i k}}. \tag{A96}$$

Equations (A93)–(A96) must be solved iteratively for $W_{T_i k}/r_k$.

The critical full island width (in r), which must be exceeded before the electron density is flattened within the magnetic separatrix of the magnetic island chain at the kth resonant surface, is[7,41]

$$W_{n_e k} = \sqrt{8}\left(\frac{D_\perp}{\chi_{\parallel i}}\right)_{r_k}^{1/4}\left(\frac{1}{\epsilon\, s\, n}\right)_{r_k}^{1/2} r_k, \tag{A97}$$

where

$$\chi_{\parallel i} = \frac{\chi_{\parallel i}^{\text{brag}}\,\chi_{\parallel i}^{\max}}{\chi_{\parallel i}^{\text{brag}} + \chi_{\parallel i}^{\max}}, \tag{A98}$$

$$\chi_{\parallel i}^{\text{brag}} = \frac{1.953\,\tau_{ii}\,v_{Ti}^2}{\sqrt{2}\,Z_{\text{eff}}}, \tag{A99}$$

$$\chi_{\parallel i}^{\max} = \frac{2\,R_0\,v_{Ti}}{\pi^{1/2}\,n\,s}\,\frac{r_k}{W_{n_e k}}. \tag{A100}$$

Equations (A97)–(A100) must be solved iteratively for $W_{n_e k}/r_k$.

d. Resonant plasma response model

Let $\chi_k = R_0\,B_0\,\hat{\chi}_k\,e^{-i\zeta_k}$, and $E_{kk'} = \hat{E}_{kk'}\,e^{-i\,\xi_{kk'}}$, where $\hat{\chi}_k > 0$, ζ_k, $\hat{E}'_{kk} > 0$, and $\xi_{kk'}$ are all real quantities. Furthermore, let $X_k = \hat{\Psi}_k\cos\varphi_k$ and $Y_k = \hat{\Psi}_k\sin\varphi_k$. The resonant plasma response model at the kth resonant surface takes the form[10,12]

$$\left(\hat{W}_k + \hat{\delta}_k\right)\mathcal{S}_k\left(\frac{dX_k}{d\hat{t}} + \hat{\varpi}_k\,Y_k\right) = f_k\,X_k + \sum_{k'=1,K}\hat{E}_{kk'}\left(\cos\xi_{kk'}\,X_{k'} - \sin\xi_{kk'}\,Y_{k'}\right) + \hat{E}_{kk}\,\hat{\chi}_k\,\cos\zeta_k, \tag{A101}$$

$$\left(\hat{W}_k + \hat{\delta}_k\right)\mathcal{S}_k\left(\frac{dY_k}{d\hat{t}} - \hat{\varpi}_k\,X_k\right) = f_k\,Y_k + \sum_{k'=1,K}\hat{E}_{kk'}\left(\cos\xi_{kk'}\,Y_{k'} + \sin\xi_{kk'}\,X_{k'}\right) + \hat{E}_{kk}\,\hat{\chi}_k\,\sin\zeta_k, \tag{A102}$$

where

$$\hat{W}_k = \frac{\mathcal{I}\,W_k}{2\,r_k} = \frac{2\,\mathcal{I}}{\epsilon_{100}\,\hat{r}_k}\left(\frac{q}{g\,s}\right)_{r_k}^{1/2}\left(X_k^2 + Y_k^2\right)^{1/4}, \tag{A103}$$

$$\hat{\delta}_k = \frac{\delta_{\text{linear}}(r_k)}{R_0\,\epsilon_{100}\,\hat{r}_k}, \tag{A104}$$

$$\mathcal{S}_k = \frac{\tau_R(r_k)}{\tau_A}, \tag{A105}$$

$$\tau_A = \left[\frac{\mu_0\,\rho(0)\,r_{100}^2}{B_0^2}\right]^{1/2}, \tag{A106}$$

$$f_k = f_{bk} + f_{ck} + f_{pk} + f_{sk}. \tag{A107}$$

Here, $\mathcal{I} = 0.8227$, $\epsilon_{100} = r_{100}/R_0$, $\hat{r} = r/r_{100}$, $\hat{r}_k = r_k/r_{100}$, and $\hat{t} = t/\tau_A$.

The perturbed bootstrap current terms in the resonant response model take the following forms:[31,42]

$$f_{bk} = f_{bek} + f_{bik}, \tag{A108}$$

$$f_{bek} = \alpha_{bek}(f_{bT_e k} + f_{bn_e k}), \tag{A109}$$

$$f_{bik} = \alpha_{bik}(f_{bT_i k} + f_{bn_i k}), \tag{A110}$$

$$f_{bT_e k} = \left(\frac{\eta_e}{1+\eta_e}\right)_{r_k}\frac{\hat{W}_k}{\hat{W}_{T_e k}^2 + \hat{\rho}_{\theta ek}^2 + \hat{W}_k^2}, \tag{A111}$$

$$f_{bn_e k} = \left(\frac{1}{1+\eta_e}\right)_{r_k}\frac{\hat{W}_k}{\hat{W}_{n_e k}^2 + \hat{\rho}_{\theta ek}^2 + \hat{W}_k^2}, \tag{A112}$$

$$f_{bT_i k} = \left(\frac{\eta_i}{1+\eta_i}\right)_{r_k}\frac{\hat{W}_k}{\hat{W}_{T_i k}^2 + \hat{\rho}_{\theta ik}^2 + \hat{W}_k^2}, \tag{A113}$$

$$f_{bn_i k} = \left(\frac{1}{1+\eta_i}\right)_{r_k}\frac{\hat{W}_k}{\hat{W}_{n_e k}^2 + \hat{\rho}_{\theta ik}^2 + \hat{W}_k^2}, \tag{A114}$$

where

$$\alpha_{bek} = -2\,\mathcal{I}\,I_g\left(\frac{\omega_{*e} + \omega_{\text{nc}e}}{\omega_\beta}\right)_{r_k}, \tag{A115}$$

$$\alpha_{b\,i\,k} = 2\,\mathcal{I}\,I_g \left[\frac{(n_i/n_e)(\omega_{*\,i} + \omega_{\mathrm{nc}\,i}) + (Z_I\,n_I/n_e)(\omega_{*\,I} + \omega_{\mathrm{nc}\,I})}{\omega_\beta} \right]_{r_k}, \tag{A116}$$

$$\omega_\beta(r) = \frac{s\,g\,B_0}{\mu_0\,n_e\,e\,R_0^2\,q}, \tag{A117}$$

$$\hat{W}_{T_e\,k} = \frac{\mathcal{I}\,W_{T_e\,k}}{2\,r_k}, \tag{A118}$$

$$\hat{W}_{T_i\,k} = \frac{\mathcal{I}\,W_{T_i\,k}}{2\,r_k}, \tag{A119}$$

$$\hat{W}_{n_e\,k} = \frac{\mathcal{I}\,W_{n_e\,k}}{2\,r_k}, \tag{A120}$$

$$\hat{\rho}_{\theta\,e\,k} = \left(\frac{\mathcal{I}\,\rho_{\theta\,e}}{2\,r} \right)_{r_k} = \left(\frac{2\,\mathcal{I}\,v_{T\,e}\,m_e\,q\,R_0}{e\,B_0\,g\,r^2} \right)_{r_k}, \tag{A121}$$

$$\hat{\rho}_{\theta\,i\,k} = \left(\frac{\mathcal{I}\,\rho_{\theta\,i}}{2\,r} \right)_{r_k} = \left(\frac{2\,\mathcal{I}\,v_{T\,i}\,m_i\,q\,R_0}{e\,B_0\,g\,r^2} \right)_{r_k}, \tag{A122}$$

and $I_g = 1.58$.

The magnetic field-line curvature terms in the resonant response model take the following forms:[31,42]

$$f_{c\,k} = \alpha_{c\,k}(f_{c\,T_e\,k} + f_{c\,n_e\,k} + f_{c\,T_i\,k} + f_{c\,n_i\,k}), \tag{A123}$$

$$f_{c\,T_e\,k} = \left(\frac{n_e}{n_e + n_i} \frac{\eta_e}{1 + \eta_e} \right)_{r_k} \frac{\hat{W}_k}{\hat{W}_{T_e\,k}^2 + \hat{W}_k^2}, \tag{A124}$$

$$f_{c\,n_e\,k} = \left(\frac{n_e}{n_e + n_i} \frac{1}{1 + \eta_e} \right)_{r_k} \frac{\hat{W}_k}{\hat{W}_{n_e\,k}^2 + \hat{W}_k^2}, \tag{A125}$$

$$f_{c\,T_i\,k} = \left(\frac{n_i}{n_e + n_i} \frac{\eta_i}{1 + \eta_i} \right)_{r_k} \frac{\hat{W}_k}{\hat{W}_{T_i\,k}^2 + \hat{W}_k^2}, \tag{A126}$$

$$f_{c\,n_i\,k} = \left(\frac{n_i}{n_e + n_i} \frac{1}{1 + \eta_i} \right)_{r_k} \frac{\hat{W}_k}{\hat{W}_{n_e\,k}^2 + \hat{W}_k^2}, \tag{A127}$$

where

$$\alpha_{c\,k} = 2\,\mathcal{I}\,I_g\,D_R(r_k). \tag{A128}$$

Here, $D_R(r)$ is the Glasser–Greene–Johnson resistive interchange stability parameter (see subsection 2 e of the Appendix).

The ion polarization terms in the resonant response model take the following forms:[31,42]

$$f_{p\,k} = \alpha_{p\,k}(f_{p\,T_i\,k} + f_{p\,n_i\,k}), \tag{A129}$$

$$f_{p\,T_i\,k} = \left(\frac{\eta_i}{1 + \eta_i} \right)_{r_k} \frac{\hat{W}_k}{(\hat{W}_{T_i\,k}^2 + \hat{W}_k^2)^2}, \tag{A130}$$

$$f_{p\,n_i\,k} = \left(\frac{1}{1 + \eta_i} \right)_{r_k} \frac{\hat{W}_k}{(\hat{W}_{n_e\,k}^2 + \hat{W}_k^2)^2}, \tag{A131}$$

where

$$\alpha_{p\,k} = 8\,\mathcal{I}^3\,I_p \left[\frac{(\omega_{*\,i} + \omega_{\mathrm{nc}\,i})\,\omega_{\mathrm{nc}\,i}}{\omega_\beta\,\omega_\Omega} \right]_{r_k}, \tag{A132}$$

$$\omega_\Omega(r) = \frac{e\,g\,B_0\,s\,q}{m_i} \tag{A133}$$

and $I_p = 1.38$.

Finally, the island saturation terms in the resonant response model take the form[43]

$$f_{s\,k} = -(0.8\,A_k^2 - 0.27\,B_k - 0.09\,A_k)\,\frac{W_k}{r_k}. \tag{A134}$$

5. Plasma angular velocity evolution

a. Evolution equations

The quantity $\hat{\varpi}_k$ that appears in Eqs. (A101) and (A102) evolves in time according to[10]

$$\hat{\varpi}_k(\hat{t}) = \hat{\varpi}_{k0} - \sum_{k'=1,K}^{p=1,\infty} \frac{m_k}{m_{k'}} \frac{y_p(\hat{r}_k)}{y_p(\hat{r}_{k'})}\,\alpha_{k',p}(\hat{t}) - \sum_{k'=1,K}^{p=1,\infty} \frac{z_p(\hat{r}_k)}{z_p(\hat{r}_{k'})}\,\beta_{k',p}(\hat{t}). \tag{A135}$$

Here, $\hat{\varpi}_{k0} = \varpi_{k0}\,\tau_A$, $y_p(\hat{r}) = J_1(j_{1,p}\,\hat{r})/\hat{r}$, and $z_p(\hat{r}) = J_0(j_{0,p}\,\hat{r})$. Moreover, ϖ_{k0} is the so-called "natural frequency" (in the absence of the RMP) at the kth resonant surface; this quantity is defined as the helical phase velocity of a naturally unstable island chain, resonant at the surface, in the absence of an RMP (or any other island chains). Furthermore, $J_m(z)$ is a standard Bessel function, and $j_{m,p}$ denotes the pth zero of this function. The time evolution equations for the $\alpha_{k,p}$ and $\beta_{k,p}$ parameters specify how the plasma poloidal and toroidal angular velocity profiles are modified by the electromagnetic torques that develop within the plasma, in response to the applied RMP, and how these modifications affect the natural frequencies. The evolution equations take the following forms:[10]

$$(1 + 2\,Q_k^2)\,\frac{d\alpha_{k,p}}{d\hat{t}} + \left(\frac{j_{1,p}^2}{\hat{\tau}_{M\,k}} + \frac{1}{\hat{\tau}_{\theta\,k}} + \frac{1}{\hat{\tau}_{\mathrm{cx}\,k}} \right) \alpha_{k,p} = \frac{m_k^2\,[y_p(\hat{r}_k)]^2}{\hat{\rho}_k\,\epsilon_{100}^2\,[J_2(j_{1,p})]^2}\,\delta\hat{T}_k, \tag{A136}$$

$$\frac{d\beta_{k,p}}{d\hat{t}} + \left(\frac{j_{0,p}^2}{\hat{\tau}_{M\,k}} + \frac{1}{\hat{\tau}_{\mathrm{cx}\,k}} \right) \beta_{k,p} = \frac{n^2\,[z_p(\hat{r}_k)]^2}{\hat{\rho}_k\,[J_1(j_{0,p})]^2}\,\delta\hat{T}_k, \tag{A137}$$

where

$$\delta\hat{T}_k = \sum_{k'=1,K} \hat{E}_{kk'}[(Y_k\,X_{k'} - X_k\,Y_{k'})\,\cos\xi_{kk'} - (X_k\,X_{k'} + Y_k\,Y_{k'})\,\sin\xi_{kk'}] + \hat{E}_{kk}\,\hat{\chi}_k\,(Y_k\,\cos\zeta_k - X_k\,\sin\zeta_k). \tag{A138}$$

Here, $Q_k = Q(r_k)$, $\hat{\rho}_k = \rho(r_k)/\rho(0)$, $\hat{\tau}_{M\,k} = r_{100}^2/[\chi_\phi(r_k)\,\tau_A]$, $\hat{\tau}_{\theta\,k} = \tau_\theta(r_k)/\tau_A$, $\hat{\tau}_{\mathrm{cx}\,k} = \tau_{\mathrm{cx}}(r_k)/\tau_A$. Moreover,

$$\tau_\theta(r) = \frac{\tau_{ii}}{\mu_{00}^i} \Big/ \left(1 + \frac{q^2\,R_0^2}{r^2\,a_{kk}} \right) \tag{A139}$$

is the poloidal flow damping timescale, and

$$\tau_{cx}(r) = \frac{1}{\langle n_n \rangle \langle \sigma v \rangle_i^{cx}} \tag{A140}$$

is the charge-exchange damping timescale. Furthermore,[44]

$$Q^2(r) = \frac{q^2 R_0^2}{2 r^2} \left(\left\langle \frac{1}{R^2} \right\rangle - \frac{1}{\langle R^2 \rangle} \right) \Big/ \left\langle \frac{|\nabla r|^2}{R^2} \right\rangle. \tag{A141}$$

b. Natural frequencies

According to linear tearing mode theory, in the absence of the RMP, the natural frequency of the tearing mode resonant at the kth resonant surface is given by[10,26]

$$\varpi_{ek} = -n \left(\omega_E + \omega_{*e} \right)_{r_k}. \tag{A142}$$

According to the nonlinear tearing mode theory, in the absence of the RMP, the natural frequency of the tearing mode resonant at the kth resonant surface is given by[10,31,42]

$$\varpi_{ik} = -n \left(\omega_E + \omega_{*i} + \omega_{nci} \right)_{r_k}. \tag{A143}$$

It is also helpful to define

$$\varpi_{Ek} = -n \left(\omega_E \right)_{r_k}. \tag{A144}$$

The EPEC model for the natural frequency is

$$\varpi_{k0} = \varpi_{Ek} + (\varpi_{ek} - \varpi_{Ek}) f_{ek} + (\varpi_{ik} - \varpi_{Ek}) f_{ik}, \tag{A145}$$

where

$$f_{ek} = f_{T_e k} + f_{n_e k}, \tag{A146}$$

$$f_{ik} = f_{T_i k} + f_{n_i k}, \tag{A147}$$

$$f_{T_e k} = \left(\frac{\eta_e}{1+\eta_e} \right)_{r_k} \frac{\hat{W}_{T_e k}^2}{\hat{W}_{T_e k}^2 + \hat{W}_k^2}, \tag{A148}$$

$$f_{n_e k} = \left(\frac{1}{1+\eta_e} \right)_{r_k} \frac{\hat{W}_{n_e k}^2}{\hat{W}_{n_e k}^2 + \hat{W}_k^2}, \tag{A149}$$

$$f_{T_i k} = \left(\frac{\eta_i}{1+\eta_i} \right)_{r_k} \frac{\hat{W}_k^2}{\hat{W}_{T_i k}^2 + \hat{W}_k^2}, \tag{A150}$$

$$f_{n_i k} = \left(\frac{1}{1+\eta_i} \right)_{r_k} \frac{\hat{W}_k^2}{\hat{W}_{n_e k}^2 + \hat{W}_k^2}. \tag{A151}$$

Note that the switchover from linear to nonlinear theory is triggered by the flattening of the local temperature and density profiles.

REFERENCES

[1] J. A. Wesson, *Tokamaks*, 4th ed. (Oxford University Press, 2011).
[2] R. J. Buttery, S. Günter, G. Giruzzi, T. C. Hender, D. Howell, G. Huysmans, R. J. LaHaye, M. Maraschek, H. Reimerdes, O. Sauter, C. D. Warrick, H. R. Wilson, and H. Zohm, Plasma Phys. Controlled Fusion **42**, B61 (2000).
[3] R. J. LaHaye, Phys. Plasmas **13**, 055501 (2006).
[4] Z. Chang, J. D. Callen, E. D. Fredrickson, R. V. Budny, C. C. Hegna, K. M. McGuire, M. C. Zarnstorff, and TFTR Group, Phys. Rev. Lett. **74**, 4663 (1995).
[5] R. J. Bickerton, J. W. Connor, and J. B. Taylor, Nat. Phys. Sci. **229**, 110 (1971).
[6] R. Carrera, R. D. Hazeltine, and M. Kotschenreuther, Phys. Fluids **29**, 899 (1986).
[7] R. Fitzpatrick, Phys. Plasmas **2**, 825 (1995).
[8] C. C. Hegna, J. D. Callen, and R. J. LaHaye, Phys. Plasmas **6**, 130 (1999).
[9] Q. Yu, S. Günter, K. Lackner, and M. Maraschek, Nucl. Fusion **52**, 063020 (2012).
[10] R. Fitzpatrick and A. O. Nelson, Phys. Plasmas **27**, 072501 (2020).
[11] R. Fitzpatrick, Phys. Plasmas **27**, 102511 (2020).
[12] R. Fitzpatrick, Phys. Plasmas **28**, 022503 (2021).
[13] R. Fitzpatrick, S.-K. Kim, and J. Lee, Phys. Plasmas **28**, 082511 (2021).
[14] H. P. Furth, J. Killeen, and M. N. Rosenbluth, Phys. Fluids **6**, 459 (1963).
[15] B. Coppi, J. M. Greene, and J. L. Johnson, Nucl. Fusion **6**, 101 (1966).
[16] P. H. Rutherford, Phys. Fluids **16**, 1903 (1973).
[17] G. Ara, B. Basu, B. Coppi, G. Laval, M. N. Rosenbluth, and B. V. Waddell, Ann. Phys. (N.Y.) **112**, 443 (1978).
[18] A. Pletzer and R. L. Dewar, J. Plasma Phys. **45**, 427 (1991).
[19] R. Fitzpatrick, Nucl. Fusion **33**, 1049 (1993).
[20] R. Fitzpatrick, R. J. Hastie, T. J. Martin, and C. M. Roach, Nucl. Fusion **33**, 1533 (1993).
[21] S. Tokuda, Nucl. Fusion **41**, 1037 (2001).
[22] D. P. Brennan, R. J. La Haye, A. D. Turnbull, M. S. Chu, T. H. Jensen, L. L. Lao, T. C. Luce, P. A. Politzer, and E. J. Strait, Phys. Plasmas **10**, 1643 (2003).
[23] A. H. Glasser, Z. R. Wang, and J.-K. Park, Phys. Plasmas **23**, 112506 (2016).
[24] R. Fitzpatrick, Phys. Plasmas **24**, 072506 (2017).
[25] S. P. Hirshman and D. J. Sigmar, Nucl. Fusion **21**, 1079 (1981).
[26] A. Cole and R. Fitzpatrick, Phys. Plasmas **13**, 032503 (2006).
[27] R. Fitzpatrick, Phys. Plasmas **29**, 032507 (2022).
[28] R. Fitzpatrick and F. L. Waelbroeck, Phys. Plasmas **12**, 022307 (2005).
[29] A. I. Smolyakov, Plasma Phys. Controlled Fusion **35**, 657 (1993).
[30] R. Fitzpatrick and F. L. Waelbroeck, Phys. Plasmas **16**, 072507 (2009).
[31] R. Fitzpatrick, Phys. Plasmas **23**, 052506 (2016).
[32] J. M. Canik, R. Maingi, T. E. Evans, R. E. Bell, S. P. Gerhardt, H. W. Kugel, B. P. LeBlanc, J. Manickam, J. E. Menard, T. H. Osborne, J.-K. Park, S. Paul, P. B. Snyder, S. A. Sabbagh, E. A. Unterberg, and NSTX Team, Nucl. Fusion **50**, 034012 (2010).
[33] W. Zhu, S. A. Sabbagh, R. E. Bell, M. Bialek, M. G. Bell, B. P. LeBlanc, S. M. Kaye, F. M. Levinton, J. E. Menard, K. C. Shaing, A. C. Sontag, and H. Yuh, Phys. Rev. Lett. **96**, 225002 (2006).
[34] C. F. Barnett, *Atomic Data for Fusion* (Oak Ridge National Laboratory, TN, 1990), Vol. 1, p. ORNL-6086.
[35] Q. M. Hu, R. Nazikian, B. A. Grierson, N. C. Logan, J.-K. Park, C. Paz-Solden, and Q. Yu, Phys. Plasmas **26**, 120702 (2019).
[36] J.-K. Park and N. C. Logan, Phys. Plasmas **24**, 032505 (2017).
[37] S. J. Zweben, J. R. Myra, A. Diallo, D. A. Russell, F. Scotti, and D. P. Stotler, Phys. Plasmas **26**, 072502 (2019).
[38] O. Meneghini, S. P. Smith, L. L. Lao, O. Izacard, Q. Ren, J. M. Park, J. Candy, Z. Wang, C. J. Luna, V. A. Izzo *et al.*, Nucl. Fusion **55**, 083008 (2015).
[39] A. H. Glasser, J. M. Greene, and J. L. Johnson, Phys. Fluids **18**, 875 (1975).
[40] P. Monier-Garbet, K. H. Burrell, F. L. Hinton, J. Kim, X. Garbet, and R. J. Groebner, Nucl. Fusion **37**, 403 (1997).
[41] S. I. Braginskii, *Reviews of Plasma Physics* (Consultants Bureau, New York, NY, 1965), Vol. I, p. 205.
[42] R. Fitzpatrick, Phys. Plasmas **25**, 082513 (2018).
[43] R. J. Hastie, F. Militello, and F. Porcelli, Phys. Rev. Lett. **95**, 065001 (2005).
[44] S. P. Hirshman, Nucl. Fusion **18**(7), 917 (1978).